Theor. Comput. Fluid Dyn. (2006) 20: 351–375
DOI 10.1007/s00162-006-0013-2

ORIGINAL ARTICLE

Boualem Khouider · Andrew J. Majda

Multicloud convective parametrizations with crude vertical structure

Received: 1 August 2005 / Accepted: 31 January 2006 / Published online: 5 May 2006

Abstract Recent observational analysis reveals the central role of three multi-cloud types, congestus, stratiform, and deep convective cumulus clouds, in the dynamics of large scale convectively coupled Kelvin waves, westward propagating two-day waves, and the Madden–Julian oscillation. The authors have recently developed a systematic model convective parametrization highlighting the dynamic role of the three cloud types through two baroclinic modes of vertical structure: a deep convective heating mode and a second mode with low level heating and cooling corresponding respectively to congestus and stratiform clouds. The model includes a systematic moisture equation where the lower troposphere moisture increases through detrainment of shallow cumulus clouds, evaporation of stratiform rain, and moisture convergence and decreases through deep convective precipitation and a nonlinear switch which favors either deep or congestus convection depending on whether the troposphere is moist or dry. Here several new facets of these multi-cloud models are discussed including all the relevant time scales in the models and the links with simpler parametrizations involving only a single baroclinic mode in various limiting regimes. One of the new phenomena in the multi-cloud models is the existence of suitable unstable radiative convective equilibria (RCE) involving a larger fraction of congestus clouds and a smaller fraction of deep convective clouds. Novel aspects of the linear and nonlinear stability of such unstable RCE's are studied here. They include new modes of linear instability including mesoscale second baroclinic moist gravity waves, slow moving mesoscale modes resembling squall lines, and large scale standing modes. The nonlinear instability of unstable RCE's to homogeneous perturbations is studied with three different types of nonlinear dynamics occurring which involve adjustment to a steady deep convective RCE, periodic oscillation, and even heteroclinic chaos in suitable parameter regimes.

Keywords Intermediate convective parametrizations · Multicloud models · Moist gravity waves · Tropical convection · Convective instability · Bifurcation · Periodic solutions · Heteroclinic orbits · Congestus clouds · Stratiform clouds · Deep convective clouds

PACS 92.60, 92.60, 92.60, 02.30, 202.60

Communicated by R. Klein

B. Khouider(✉)
Mathematics and Statistics, University of Victoria,
PO BOX 3045 STN CSC, Victoria, BC, Canada V8W 3P4
E-mail: khouider@math.uvic.ca

A. J. Majda
Department of Mathematics and Center for Atmosphere/Ocean Sciences,
Courant Institute, New York University, 251 Mercer Street,
New York, NY 10012, USA

1 Introduction

Observational data indicate that tropical deep convection is organized on a hierarchy of scales ranging from hundreds of kilometers due to mesoscale organized squall lines to intraseasonal oscillations over planetary scales of order 40,000 km [1–3]. The present practical models for prediction of both weather and climate involve general circulation models (GCM) where the physical equations for these extremely complex flows are discretized in space and time and the effects of unresolved processes are parametrized according to various recipes [4,5]. With the current generation of supercomputers, the smallest possible mesh spacings are roughly 50–100 km for short-term tropical weather simulations and of 200–300 km for short-term climate simulations. With such coarse mesh spacing, despite much progress in the parametrization of tropical convection, the current generation of GCMs [4,5] still fails to reproduce most of the significant features of the observational record [1–3] regarding tropical convection [4,5]. Thus, given the importance of the tropics for short-term climate, new strategies for parametrizing the unresolved effects of tropical convection are very important.

In particular, contemporary general circulation models (GCMs) often perform poorly in parameterizing and/or resolving the observed large scale features of organized tropical convection such as convectively coupled waves as well as their impact on the planetary scale tropical circulation [6,7]; the reasons for such poor performance are not well understood.

Simplified models with crude vertical resolution, typically involving a single baroclinic vertical mode, have been used for theoretical and numerical studies of various strategies for parameterizing moist convection and convectively coupled waves [8–16]. Two types of models have dominated the arena of tropical moist convection: convergence-driven models and quasi-equilibrium models. Convergence models date back to the work of Charney and Eliassen [17], followed by Yamasaki [18], Hayashi [19], and Lindzen [20]. The convergence models, also called convective instability of second kind (CISK) models, sustain convection through large reservoirs of convectively available potential energy (CAPE) driven by low-level convergence. Such models exhibit extreme sensitivity to grid scale behavior and linearized stability analysis reveals the undesirable feature of catastrophic instability with increasingly larger growth rates on the smallest scales [12,13]. In the quasi-equilibrium thinking, first introduced by Arakawa and Schubert [21], one assumes a large scale quasi-equilibrium state where CAPE is nearly constant and deep convection acts as an energy regulator in restoring quickly the equilibrium by consuming any excess of CAPE. The triggering and the amplification of convection in quasi-equilibrium models rely on boundary layer variables and surface fluxes. Indeed, such quasi-equilibrium models are linearly [10] and even nonlinearly stable [16]. The most popular mechanism used in concert with the quasi-equilibrium models to create instability is wind induced surface heat exchange (WISHE) [8,22].

Recent analysis of observations over the warm pool in the tropics reveals the ubiquity of three cloud types above the boundary layer: shallow congestus clouds, stratiform clouds, and deep penetrative cumulus clouds [23,24]. Furthermore, recent analysis of convectively coupled waves on the large scales reveals a similar multi-cloud convective structure with leading shallow congestus cloud decks which moisten and precondition the lower troposphere followed by deep convection and finally trailing decks of stratiform precipitation; this structure applies to the eastward propagating convectively coupled Kelvin waves [3,25] and westward propagating 2-day waves [26] which reside on equatorial synoptic scales of order 1,000–3,000 km in the lower troposphere as well as the planetary scale Madden–Julian oscillation [27,28]. An inherently multi-scale theory for the Madden–Julian oscillation with qualitative agreement with observations which is based on these three cloud types has been developed recently [29,30]. While there is no doubt that WISHE plays an important role in hurricane development [31,32], there is no observational evidence directly linking the structure of convectively coupled Kelvin waves and 2-day waves to WISHE.

Besides providing intermediate models for parametrization of moist convection, detailed models with crude vertical resolution are also important for explaining the observational record. Despite the observational evidence, none of the models with a single vertical mode mentioned earlier account for the multi-mode nature of tropical convection and the importance of the different cloud types; shallow/congestus, stratiform and deep-penetrative cumulus clouds. They are concentrated solely on the deep-penetrative convection. Intermediate model parametrizations with two convective heating modes systematically representing, a deep-convective mode and a stratiform mode, have first appeared in the work of Mapes [33]. Majda and Shefter [34] (hereafter MS) proposed a much simpler systematic version of Mapes' model based on a Galerkin projection of the primitive equations onto the first two linear-baroclinic modes yielding a set of two shallow water systems. The first baroclinic system is heated by the deep convective clouds while the second baroclinic system is heated aloft by the stratiform clouds. Linear stability analysis of this model convective parametrization revealed a

mechanism of stratiform instability independent of WISHE [34,35]. Direct numerical simulations carried out in [35] revealed the resemblance of many features of the moist gravity waves for the MS model and the real world convective superclusters as depicted in [35] and in observational papers (e.g. [25]). One visible shortcoming of the MS model is however its short-cutting of the role of the shallow/congestus heating as in the early Mapes' model. Also, inherited from the quasi-equilibrium school [12,36], the Majda-Shefter model [34] uses very sensitive parameters which are nonphysically kept fixed/constant and spatially homogeneous, such as the precipitation efficiency and the area fraction of deep convection.

Recently, the authors have developed a new multi-cloud model convective parametrization, within a framework similar to the MS model [34] involving crude vertical resolution with two vertical baroclinic modes [37]. In addition to the deep convective and stratiform clouds, the present model carries cumulus congestus clouds which serve to heat the second baroclinic mode from below and cool it from above as in actual congestus cloud decks. The new model is based on a self-consistent derivation and it avoids many of the commonly used ad hoc parameters. We systematically derived an equation for the vertically integrated water vapor with mean vertical background moisture profile forced by both the first baroclinic and second baroclinic (low-level) convergence within the physical constraints of conservation of vertically integrated moist static energy. Also the new model takes into account the dryness and moistness of the middle troposphere through a varying-inhomogeneous switch parameter, Λ, in order to shut off or favor deep convection and to increase or decrease the downdrafts from the cooling associated with evaporation of shallow clouds and stratiform rain. Moreover, the congestus convection is amplified whenever the middle troposphere is too dry to sustain deep convection and is shut off completely when deep-convection is at its maximum.

Linear stability analysis about a standard radiative convective equilibrium (RCE) solution performed in [37] revealed scale selective instability of convectively coupled gravity waves moving at 15–20 m/s at the planetary and synoptic scales. The growth rates and the precise range of instability depend strongly on new features in the model such as the strength of the lower tropospheric coupling of the deep convective parametrization, through the second baroclinic potential temperature and the second baroclinic moisture convergence. The heating and fluid dynamical fields of these moist gravity waves are similar to those encountered in the MS model which are reminiscent of the moist Kelvin waves as observed, e.g. by Wheeler and Kiladis [3] and Straub and Kiladis [25], including their eastward propagation speed, the tilt in zonal wind and temperature, the upward motion dominating the heating region, the trailing stratiform part, etc. A notable new feature of the present models, also present in observations, is congestus clouds leading to moistening of the lower troposphere as preconditioning for deep convection. The budget analysis presented in [37] indicates that the basic instability operating in the new multi-cloud models without WISHE is completely different from the stratiform instability of Majda and Shefter [34].

Numerical simulations of the new multi-cloud parametrizations [38,39] reveal an important role for nonlinear switches in the model with chaotic intermittent and turbulent regimes of nonlinear dynamics exhibiting large scale organization of convectively coupled waves which captures many features of the observational record in a qualitative fashion.

The contents of the remainder of the paper are summarized next. In Sect. 2, the basic multi-cloud model parametrization is reviewed. Section 3 shows the relationship between the present multi-cloud parametrization with crude vertical resolution and other simpler model parametrizations in various limiting regimes. The authors briefly remarked in [37] that regimes of RCE with strong congestus clouds and little deep convection in a dry middle troposphere are linearly unstable to even homogeneous perturbations. Section 4 reviews the basic RCE solutions and develops the new phenomena that occur in this regime in detail including the nonlinear development of homogeneous perturbations. The remarkable variety of new convectively coupled moisture waves of linear instability are discussed in Sect. 5 while Sect. 6 summarizes the results presented herein and concludes the paper. Finally, a detailed pedagogical derivation of the vertical average moisture equation utilized in the multicloud parametrizations is given in the appendix at the end.

2 The multicloud model parametrization

2.1 The dynamical core

The dynamical core of the model convective parametrization proposed here consists of two coupled shallow water systems. A direct heating mode forced by a bulk precipitation rate from deep penetrative clouds and a second baroclinic mode forced by both stratiform heating and congestus heating.

$$\begin{aligned}
\frac{\partial \mathbf{v}_j}{\partial t} + \bar{\mathbf{U}} \cdot \nabla \mathbf{v}_j + \beta y \mathbf{v}_j^{\perp} - \nabla \theta_j &= -C_d(u_0)\mathbf{v}_j - \frac{1}{\tau_W}\mathbf{v}_j \\
\frac{\partial \theta_1}{\partial t} + \bar{\mathbf{U}} \cdot \nabla \theta_1 - \operatorname{div} \mathbf{v}_1 &= \frac{\pi}{2\sqrt{2}} P + S_1 \\
\frac{\partial \theta_2}{\partial t} + \bar{\mathbf{U}} \cdot \nabla \theta_2 - \frac{1}{4}\operatorname{div} \mathbf{v}_2 &= \frac{\pi}{2\sqrt{2}}(-H_{\mathrm{s}} + H_{\mathrm{c}}) + S_2.
\end{aligned} \tag{1}$$

The equations in (1) are obtained by a Galerkin projection of the hydrostatic primitive equations with constant buoyancy frequency onto the first two baroclinic modes. More details of their derivation are found in [16,34,40]. In (1), $\mathbf{v}_j = (u_j, v_j)_{j=1,2}$ represent the first and second baroclinic velocities assuming $G(z) = \sqrt{2}\cos\left(\frac{\pi z}{H_{\mathrm{T}}}\right)$ and $G(2z) = \sqrt{2}\cos\left(\frac{2\pi z}{H_{\mathrm{T}}}\right)$ vertical profiles, respectively, while θ_j, $j = 1, 2$ are the corresponding potential temperature components with the vertical profiles $G'(z) = \sqrt{2}\sin\left(\frac{\pi z}{H_{\mathrm{T}}}\right)$ and $2G'(2z) = 2\sqrt{2}\sin\left(\frac{2\pi z}{H_{\mathrm{T}}}\right)$, respectively. Therefore, the total velocity field is approximated by

$$\mathbf{V} \approx \bar{\mathbf{U}} + G(z)\mathbf{v}_1 + G(2z)\mathbf{v}_2; \quad w \approx -\frac{H_{\mathrm{T}}}{\pi}\left[G'(z)\operatorname{div}\mathbf{v}_1 + \frac{1}{2}G'(2z)\operatorname{div}\mathbf{v}_2\right]$$

where $\mathbf{V}$ is the horizontal velocity and w the vertical velocity. The total potential temperature is given approximately by

$$\Theta \approx z + G'(z)\theta_1 + 2G'(2z)\theta_2.$$

Here $H_{\mathrm{T}} \approx 16\,\mathrm{km}$ is the height of the tropical troposphere with $0 \le z \le H_{\mathrm{T}}$ and $\mathbf{v}_j^{\perp} = (-v_j, u_j)$ while $\bar{\mathbf{U}}$ is the incompressible barotropic wind which is set to zero hereafter, for the sake of simplicity. In (1), $P \ge 0$ models the heating from deep convection while H_{s}, H_{c} are the stratiform and congestus heating rates. Conceptually, the direct heating mode has a positive component and serves to heat the whole troposphere and is associated with a vertical shear flow. The second baroclinic mode is heated by the congestus clouds, H_{c}, from below and by the stratiform clouds, H_{s}, from above and therefore cooled by H_{c} from above and by H_{s} from below. It is associated with a jet shear flow in the middle troposphere [34,35,37].

For simplicity, the nonlinear interactions between the first and second baroclinic modes are ignored but they can be easily derived and incorporated into the equations [41–43]. The terms S_1 and S_2 are the radiative cooling rates associated with the first and second baroclinic modes respectively.

The system of equations in (1) is augmented by an equation for the boundary layer equivalent potential temperature, θ_{eb}, and another for the vertically integrated moisture content, q.

$$\begin{aligned}
\frac{\partial \theta_{\mathrm{eb}}}{\partial t} &= \frac{1}{h_{\mathrm{b}}}(E - D) \\
\frac{\partial q}{\partial t} + \bar{\mathbf{U}} \cdot \nabla q + \operatorname{div}\left((\mathbf{v}_1 + \tilde{\alpha}\mathbf{v}_2)q\right) + \tilde{Q}\operatorname{div}(\mathbf{v}_1 + \tilde{\lambda}\mathbf{v}_2) &= -P + \frac{1}{H_{\mathrm{T}}}D
\end{aligned} \tag{2}$$

In (2), $h_{\mathrm{b}} \approx 500\,\mathrm{m}$ is the height of the moist boundary layer while $\tilde{Q}$, $\tilde{\lambda}$, and $\tilde{\alpha}$ are parameters associated with a prescribed moisture background and perturbation vertical profiles. According to the first equation in (2), θ_{eb} changes in response to the downdrafts, D, and the sea surface evaporation E. Here the term downdraft refers to the subsiding air resulting from evaporative cooling of congestus clouds and stratiform rain in the middle of the troposphere which therefore results in the moistening of the middle troposphere (increasing q) and drying and cooling the boundary layer by bringing low θ_{e} from aloft. The troposphere moisture equation for q is derived from the bulk water vapor budget equation by imposing a moisture stratification-like background vertical profile $q_{\mathrm{v}} = Q(z) + q$. We give a detailed pedagogical derivation of this equation in the Appendix starting from the equations of bulk cloud microphysics both for its importance and to illustrate the systematic reduced modeling procedure. The approximate numerical values of $\tilde{\lambda} = 0.8$ and $\tilde{\alpha} = 0.1$, follow directly from the derivation, while the coefficient $\tilde{Q}$ arises from the background moisture gradient. We use the standard value $\tilde{Q} \approx 0.9$ [16,36].

In full generality, the parametrizations in (1) and (2) automatically have conservation of an approximation to vertically integrated moist static energy. Notice that, the precipitation rate in (2), balances the vertical

average of the total convective heating rate in (1), therefore leading to the conservation of the vertical average of the equivalent potential temperature $\langle\theta_e\rangle = \langle Q(z)\rangle + q + \langle\Theta\rangle + \frac{h_b}{H_T}\theta_{eb}$ when the external forces, namely, the radiative cooling rates, S_1, S_2, and the evaporative heating, E, are set to zero. Also note that the sensible heating flux has been ignored in (1) for simplicity since this is a relatively small contribution in the tropics. Here and elsewhere in the text $\langle f\rangle \equiv (1/H_T)\int_0^{H_T} f(z)\,dz$.

The equations in (1) and (2) for the prognostic variables $q, \theta_{eb}, \theta_j, \mathbf{v}_j$, $j = 1, 2$, are written in non-dimensional units where the equatorial Rossby deformation radius, $L_e \approx 1{,}500$ km is the length scale, the first baroclinic dry gravity wave speed, $c \approx 50$ m/s, is the velocity scale, $T = L_e/c \approx 8$ h is the associated time scale, and the dry-static stratification $\bar{\alpha} = \frac{H_T N^2 \theta_0}{\pi g} \approx 15$ K is the temperature unit scale. The basic bulk parameters of the model are listed in Table 1 for the reader's convenience.

2.2 The convective parametrization

The surface evaporative heating, E, in (2) obeys an adjustment equation toward the boundary layer saturation equivalent potential temperature, θ^*_{eb},

$$\frac{1}{h_b}E = \frac{1}{\tau_e}(\theta^*_{eb} - \theta_{eb}) \tag{3}$$

with τ_e is the evaporative time scale. The value of θ^*_{eb} on a warm ocean surface is fixed such that at radiative convective equilibrium (RCE) we have $\theta^*_{eb} - \bar{\theta}_{eb} = 10$ K, according to the Jordan sounding [44].

Besides the second baroclinic moisture advection in (2), the originality of the present model resides in a new treatment of the deep convective heating/precipitation, P, and the downdrafts, D, as well as the introduction of the congestus heating, H_c, into the θ_2 equation. The middle tropospheric equivalent potential temperature anomaly is defined approximately by

$$\theta_{em} \approx q + \frac{2\sqrt{2}}{\pi}(\theta_1 + \alpha_2\theta_2) \tag{4}$$

where $\alpha_2 = 0.1$. Notice that the coefficient $2\sqrt{2}/\pi$ in (4) results from the vertical average of the first baroclinic potential temperature, $\sqrt{2}\theta_1 \sin(\pi z/H_T)$, while the small value for α_2 adds a non-zero contribution from θ_2 to θ_{em} to include its contribution from the lower middle troposphere although its vertical average is zero.

Following [37], we use a switch parameter Λ which serves as a measure for the moistness and dryness of the middle troposphere [31]. When the discrepancy between the boundary layer and the middle troposphere equivalent potential temperature is above some fixed threshold, θ^+, the atmosphere is defined as dry. Moist parcels rising from the boundary layer will have their moisture quickly diluted by entrainment of dry air, hence losing buoyancy and stop to convect. In this case, we set $\Lambda = 1$ which automatically inhibits deep convection in the model (see below). When this discrepancy is below some lower value, θ^-, we have a relatively moist

Table 1 Bulk constants in two layer mode model

$H_T = 16$ km: height or the tropical troposphere
$\tilde{Q} = 0.9$: moisture stratification factor
$\tilde{\lambda} = 0.8$: $2n$ baroclinic relative contribution to the moisture convergence associated with the moisture background
$\tilde{\alpha} = 0.1$: $2n$ baroclinic relative contribution to the moisture (nonlinear) convergence associated with the moisture anomalies
$\tau_W = 75$ days: Rayleigh-wind friction relaxation time
$\tau_R = 50$ days: Newtonian cooling relaxation time
$c_d = 0.001$: boundary layer turbulence momentum friction
$L_e \approx 1500$ km: equatorial deformation radius, length scale
$c \approx 50$ m/s: speed of the first baroclinic gravity wave, velocity scale
$T = L_e/c \approx 8$ h: time scale
$\bar{\alpha} \approx 15$ K: dry static stratification, temperature scale
$N = 0.01\text{s}^{-1}$: Brunt–Vaisala buoyancy frequency
$\theta_0 = 300$ K: reference temperature
$h_b = 500$ m: boundary layer height
$\bar{X}$: RCE value of the variable X
$\alpha_2 = 0.1$: relative contribution of θ_2 to the middle troposphere θ_e

atmosphere and we set $\Lambda = \Lambda^* < 1$. The lower threshold Λ^* can basically take any value between zero and one and here $\Lambda^* = 0.2$ to guarantee a non-zero downdraft fraction minimum within the regions of deep convection. We are avoiding the value $\Lambda^* = 0$ here because we believe it is unphysical; even if a given grid cell is deep convecting at its maximum, it doesn't mean that there is deep convection all over the cell, there should be some congestus, stratiform, and/or even clear sky regions within that cell. The function Λ is then interpolated (linearly) between these two values. More precisely we set

$$\Lambda = \begin{cases} 1 & \text{if } \theta_{\rm eb} - \theta_{\rm em} > \theta^+ \\ A(\theta_{\rm eb} - \theta_{\rm em}) + B & \text{if } \theta^- \le \theta_{\rm eb} - \theta_{\rm em} \le \theta^+ \\ \Lambda^* & \text{if } \theta_{\rm eb} - \theta_{\rm em} < \theta^-. \end{cases} \tag{5}$$

Here $\theta^+ = 20\,\mathrm{K}$ and $\theta^- = 10\,\mathrm{K}$ while A and B are fitting constants guaranteeing continuity of Λ. The value of θ^- is chosen according to the Jordan sounding (Fig. 3.5 from [44]). It represents a threshold below which the free troposphere is locally moist and "accepts" only deep convection while the value of $\theta^+ = 20\,\mathrm{K}$ is somehow arbitrary.

Therefore, the precipitation, P, and the downdrafts, D, obey

$$P = \frac{1-\Lambda}{1-\Lambda^*} P_0 \quad \text{and} \quad D = \Lambda D_0 \tag{6}$$

while the stratiform and congestus heating rates, $H_{\rm s}$ and $H_{\rm c}$, solve the relaxation-type equations

$$\frac{\partial H_{\rm s}}{\partial t} = \frac{1}{\tau_{\rm s}} (\alpha_{\rm s} P - H_{\rm s}) \tag{7}$$

and

$$\frac{\partial H_{\rm c}}{\partial t} = \frac{1}{\tau_{\rm c}} \left(\alpha_{\rm c} \frac{\Lambda - \Lambda^*}{1-\Lambda^*} \frac{D}{H_{\rm T}} - H_{\rm c} \right), \tag{8}$$

respectively. Notice that, as anticipated above, when the middle troposphere is dry, $\Lambda = 1$, deep convection is completely inhibited, even if P_0, i.e, CAPE is positive, whereas congestus heating is favored. In the absence of deep convection the downdrafts are interpreted as the subsidence associated with the detrainment of shallow clouds. In this sense the shallow clouds serve to moisten and precondition the middle troposphere to sustain deep convection by lowering Λ in the model via both the increase of q and the decrease of $\theta_{\rm eb}$. The situation is somewhat inverted during the deep convective episodes when $\Lambda = \Lambda^*$. Nevertheless, when this downdraft minimum fraction is reached, the downdraft will increase because of increasing stratiform heating, $H_{\rm s}$, and the vanishing congestus heating, $H_{\rm c}$ (because of the factor $(\Lambda - \Lambda^*$ in Eq. 8).

Moreover, the dry atmosphere increases the downdrafts, D, and promotes boundary layer clouds. This also is well reflected in the model.

The quantities P_0 and D_0 represent respectively the maximum allowable deep convective heating/precipitation and downdrafts, independent of the value of the switch function Λ. Notice that conceptually the model is not bound to any type of convective parametrization. A Betts–Miller relaxation type parametrization as well as a CAPE parametrization can be used to setup a closure for P_0. Indeed, here we use some combination of the two parametrization concepts. Recall that a Betts–Miller type parametrization consists of relaxing the moisture q (and/or the temperature) toward a fixed vertical profile, $\hat{q}$, (typially a tropical sounding or a moist adiabat) over some convective relaxation time $\tau_{\rm conv}$ [45]. A CAPE parametrization, on the other hand, is based on the kinetic energy available for deep convection which is directly converted into upward motion whenever deep convection is triggered. Recall also that CAPE is computed as the vertical integral of the buoyancy of the rising moist parcel which is proportional to the difference between the boundary layer and the environmental saturation equivalent potential temperatures, $\theta_{\rm eb} - \theta^*_{\rm eb}$ [46]. Furthermore, $\theta^*_{\rm eb}$ anomalies are often approximated by some linear function of the tropospheric dry potential temperature (e.g. [13]). Here we let

$$P_0 = \frac{1}{\tau_{\rm conv}} \left(a_1 \theta_{\rm eb} + a_2 (q - \hat{q}) - a_0 (\theta_1 + \gamma_2 \theta_2) \right)^+ \tag{9}$$

where $\hat{q}$ is a threshold constant value measuring a significant fraction of the tropospheric saturation and $\tau_{\rm conv}, a_1, a_2, a_0$ are parameters specified below and in Table 2 [15,16]. In particular the coefficient a_0, which is somewhat related to the inverse buoyancy relaxation time of Fuchs and Raymond [15], is an important

Table 2 Parameters in the convective parameterization

θ^*_{eb}: boundary layer saturation equivalent potential temperature
$\tau_e \approx 8$ h or 9 days: evaporative time scale in the boundary layer
$\theta^{\pm} = 10, 20$ K: temperature thresholds used to define the switch function Λ
$\Lambda^* = 0.2$: lower threshold of the switch function Λ
A, B: linear fitting constants interpolating the switch function Λ
$\tau_s = 3$ h: stratiform heating adjustment time
$\alpha_s = 0.25$: stratiform heating adjustment coefficient
$\tau_c = 1$ h: congestus heating adjustment time
$\alpha_c = 0.5$ (varies): congestus heating adjustment coefficient
$a_0 = 7.5$ (varies): inverse buoyancy time scale of convective parametrization
$a_1 = 0.1$ (varies): relative contribution of θ_{eb} to the convective parametrization
$a_2 = 0.9$ (varies): relative contribution of q to the convective parametrization
$\tau_{conv} = 2$ h: deep convective reference time scale
$\hat{q}$: Threshold beyond which condensation takes place in Betts–Miller scheme
$\gamma_2 = 0.1$ (varies): relative contribution of θ_2 to the convective parametrization (strength of lower troposphere coupling)
$\bar{\theta}_{eb} - \bar{\theta}_{em} = 14$ K: discrepancy between boundary and middle tropospheric equivalent potential temperature at RCE.
m_0 (value is set by RCE): scaling of downdraft mass flux
$\mu_2 = 0.5$: relative contribution of stratiform and congestus mass flux anomalies

parameter to vary. The parameter γ_2, which couples θ_2 to P_0 is also varied to assess the effects of the lower troposphere temperature variation on the parametrizations; a relatively warm lower troposphere will promote evaporation and detrainment of cumulus clouds. Thus, it should result in a weakening of the deep convection.

The downdrafts are closed by

$$D_0 = \frac{m_0}{\bar{P}} \left(\bar{P} + \mu_2(H_s - H_c)\right)^+ (\theta_{eb} - \theta_{em}) \tag{10}$$

where m_0 is a scaling of the downdraft mass flux and $\bar{P}$ is a prescribed precipitation/deep convective heating at radiative convective equilibrium. Here μ_2 is a parameter allowing for stratiform and congestus mass flux anomalies [34,35]. Finally the radiative cooling rates, S_1, S_2 in (1) are given by a simple Newtonian cooling model

$$S_j = -Q^0_{R,j} - \frac{1}{\tau_R}\theta_j, \quad j = 1, 2 \tag{11}$$

where $Q^0_{R,j}$, $j = 1, 2$ are the radiative cooling rates at RCE. The basic constants in the model convective parametrization and the typical values utilized here are given in Table 2. The physical features incorporated in the multi-cloud model are discussed in detail in [37].

3 Formal limit regimes and related model parametrizations

It is interesting to rewrite the multi-cloud parametrization from Sect. 2 in a fashion where the relevant time scales of central physical processes are more explicit. We introduce the boundary layer to free troposphere aspect ratio,

$$R = \frac{h_b}{H_T} = \frac{500\,\text{m}}{16\,\text{m}} = \frac{1}{32} \approx 0.03 \tag{12}$$

and the downdraft time scale, τ_D, with

$$\tau_D = \frac{h_b}{m_0} \tag{13}$$

where m_0 is the downdraft mass flux from (10). We also use (9), (10) in (6) to rewrite the deep convective heating and downdraft mass flux as

$$P = \tau_{conv}^{-1}\tilde{P} \tag{14}$$

and

$$\frac{D}{h_b} = \tau_D^{-1}\tilde{D} = \tau_D^{-1}\tilde{m}(\theta_{eb} - \theta_{em}) \tag{15}$$

where the definitions of the nonlinear functions $\tilde{P}$, $\tilde{D}$, $\tilde{m}$ are clear from (6), (9), (10). Similarly with (12), (13) and (15) the coefficient in (8) is recast as

$$\alpha_c \frac{\Lambda - \Lambda^*}{1 - \Lambda^*} \frac{D}{H_T} = \frac{R}{\tau_D}\tilde{\alpha}_c\tilde{D}. \tag{16}$$

With the above preliminary definitions and ignoring the barotropic advection, the multi-cloud model convective parametrization is rewritten as given by

$$\begin{aligned}
\frac{\partial \theta_{eb}}{\partial t} &= \tau_e^{-1}(\theta_{eb}^* - \theta_{eb}) - \tau_D^{-1}\tilde{m}(\theta_{eb} - \theta_{em}) \\
\frac{\partial q}{\partial t} + \mathrm{div}\big((\mathbf{v}_1 + \tilde{\alpha}\mathbf{v}_2)q + \tilde{Q}\ \mathrm{div}(\mathbf{v}_1 + \tilde{\lambda}\mathbf{v}_2)\big) &= -\tau_{conv}^{-1}\tilde{P} + \frac{R}{\tau_D}\tilde{m}\ (\theta_{eb} - \theta_{em}) \\
\frac{\partial H_c}{\partial t} &= \tau_c^{-1}\left(\frac{R}{\tau_D}\tilde{\alpha}_c\tilde{m}(\theta_{eb} - \theta_{em}) - H_c\right) \\
\frac{\partial H_s}{\partial t} &= \tau_s^{-1}\left(\alpha_s\tau_{conv}^{-1}\tilde{P} - H_s\right)
\end{aligned} \tag{17}$$

together with the temperature and momentum equations in (1).

The important time scales for the key processes in the parametrization are the two for the boundary layer moist processes involving evaporation and downdrafts, τ_e, τ_D, and the three time scales for the three cloud types, congestus, stratiform, and deep convective, τ_c, τ_s, τ_{conv}. Actually, with the nondimensionalization discussed at the end of Sect. 2.1, these time scales are ratios with the standard equatorial gravity wave time scale, $T_E \approx 8\,\mathrm{h}$; we ignore this distinction below. We show below in Sect. 4.1 that standard values for an RCE based on the Jordan sounding yield $\tau_e \approx 8\,\mathrm{h}$. Clearly, the ratio of the times scales, τ_D/τ_e can be found for a given RCE by evaluating the right hand side of the first equation in (17) at RCE. For the standard RCE utilized in Khouider and Majda [37,39], this procedure yields that $\tau_D \approx \tau_e \approx 8\,\mathrm{h}$. The values of τ_e and τ_D for a wide range of representative RCE's in a reasonable physical range are given in Table 3. On the other hand, the adjustment times for the three cloud types in the parametrization can vary over a wide range of times comparable to τ_e with

$$\begin{aligned}
&1\,\mathrm{h} \le \tau_c, \tau_s \le 8\,\mathrm{h} \\
&2\,\mathrm{h} \le \tau_{conv} \le 8\,\mathrm{h}.
\end{aligned} \tag{18}$$

Time scales in the shorter range typically are utilized in contemporary model convective parametrizations [16, 33,37–40] mimicking the adjustment time scales used in GCM's [45,47]. On the other hand, recent interpretations of observations [48] suggested longer adjustment times, at least for τ_{conv} at the upper limit in (18), $\tau_{conv} = 8\,\mathrm{h} \approx T_E$; we have included the upper limit for τ_c, τ_s in (18) in order to keep the possibility of larger time scales for these variables, too. Thus, it is interesting to explore the behavior of the multi-cloud parametrizations in the range of parameters in (18); this is done briefly in Sects. 4 and 5 below. Obviously, in regimes of parameters where τ_c, $\tau_s << T_E$, τ_D, τ_e, τ_{conv}, formally, one can replace the two dynamic equations in (17) for H_c and H_s by their equilibrium limits but in general the above discussion shows that all the time scales in (17) should be regarded as roughly comparable.

Table 3 Typical radiative convective equilibria (RCE) in the multi-cloud parametrizations. Notice that positive $Q_{R,2}^0$ values correspond to RCE's where the congestus heating dominate the stratiform heating

$\frac{2\sqrt{2}}{\pi}Q_{R,0}^1$ (K/day)	τ_e (h)	$\bar{\theta}_{eb} - \bar{\theta}_{em}$	τ_D (h)	$\frac{2\sqrt{2}}{\pi}Q_{R,2}^0$ (K/day)
0.5	16.9253	14	12.6296	−0.0225
		19	26.6268	0.0900
1	8.4626	14	6.3148	−0.0450
		19	13.3134	0.1801
2	4.2313	14	3.1574	−0.0900
		19	6.6567	0.3601

3.1 Model parametrizations with a simple vertical baroclinic mode

The simplest limiting case of the multi-cloud parametrization is simply to arrange the parameters to decouple the second baroclinic mode from the active dynamics [35]. Thus, we set $\tilde{\lambda}, \tilde{\alpha} = 0$ in the second equation in (17), $\gamma_2 = 0$ in (9) defining P_0, and $\alpha_2 = 0$ in the formula from (4) for the middle troposphere equivalent potential temperature so that

$$\theta_{\rm em} = q + \frac{2\sqrt{2}}{\pi}\theta_1. \tag{19}$$

Then the active equations in the multicloud parametrization consist of the four equations for $\theta_{\rm eb}, q, H_{\rm c}, H_{\rm s}$ in (17) coupled to the equations for θ_1 and $\mathbf{v}_1$ involving the potential temperature and velocity of the first baroclinic mode. However, one should keep in mind that linear stability analysis and nonlinear simulations reveal an important role in the dynamics for the multicloud parametrization with the more realistic values $\tilde{\lambda} = 0.8, \gamma_2 = 0.1$, allowing for second baroclinic moisture convergence and lower middle tropospheric destabilization through second baroclinic cooling. For a comparison of these effects with the decoupled values $\tilde{\lambda} = 0, \gamma_2 = 0$, the interested reader is referred to the detailed discussion in those papers [37–39].

A further, more drastic simplification occurs if the contribution from both stratiform and congestus heating/cooling on the downdrafts are suppressed by setting $\mu_2 = 0$ in the formula in (10) in addition to the above simplifications. The stratiform and congestus heating terms, $H_{\rm s}$, $H_{\rm c}$ from (17) completely decouple and a convective parametrization for the first baroclinic mode alone results with the four equations

$$\begin{aligned}
\frac{\partial \theta_{\rm eb}}{\partial t} &= \tau_{\rm e}^{-1}(\theta_{\rm eb}^* - \theta_{\rm eb}) - \tau_{\rm D}^{-1}\tilde{D} \\
\frac{\partial q}{\partial t} + \operatorname{div}\left(\mathbf{v}_1(q + \tilde{Q})\right) &= -\tau_{\rm conv}^{-1}\tilde{P} + \frac{R}{\tau_{\rm D}}\tilde{D} \\
\frac{\partial \theta_1}{\partial t} - \operatorname{div}\mathbf{v}_1 &= \frac{\pi}{2\sqrt{2}}P + S_1 \\
\frac{\partial \mathbf{v}_1}{\partial t} + \beta y \mathbf{v}_1^{\perp} - \nabla\theta_j &= -C_{\rm d}(u_0)\mathbf{v}_1 - \frac{1}{\tau_W}\mathbf{v}_1
\end{aligned} \tag{20}$$

Compared to early first baroclinic modes [11–13], novel features in (20) arise due to the nonlinear dependence, $\Lambda(\theta_{\rm eb} - \theta_{\rm em})$, in (5) for both $\tilde{P}$ and $\tilde{D}$ which allows for the effects of a dry middle troposphere on convection as well as the nonlinear moisture advection, $\operatorname{div}(\mathbf{v}_1 q)$ in the second equation in (20). In particular, the system in (20) avoids the use of constant area fraction and precipitation efficiency parameters. The simplified models in (20) are interesting for further mathematical analysis beyond that in Frierson et al. [16]; a linearized stability analysis for (20) with a special choice of P_0 from (9) and $\Lambda = \Lambda_0$ with Λ_0 constant, i.e., a deep convective RCE, can be found in [13].

Finally, we demonstrate how the simplest moisture models in Neelin and Zeng [40], and Frierson et al. [16] can be derived from (20) with further simple approximations. First, we note that by combining the first two equations in (20), $q + R\theta_{\rm eb}$ satisfies

$$\frac{\partial}{\partial t}(q + R\theta_{\rm eb}) + \operatorname{div}\left(\mathbf{v}_1(q + \tilde{Q})\right) = \frac{R}{\tau_{\rm e}}(\theta_{\rm eb}^* - \theta_{\rm eb}) - \tau_{\rm conv}^{-1}\tilde{P}. \tag{21}$$

Next, we assume that

$$\frac{\partial}{\partial t}(q + R\theta_{\rm eb}) = \frac{\partial \langle q\rangle_{\rm b}}{\partial t} \tag{22}$$

where $\langle q\rangle_b$ is the vertically averaged moisture (including a contribution from the boundary layer)

$$\langle q\rangle_{\rm b} = Rq_{\rm b} + q \tag{23}$$

and also

$$\theta_{\rm eb}^* - \theta_{\rm eb} = \theta_{\rm b}^* - \theta_{\rm b} + q_{\rm b}^* - q_{\rm b} \approx q^* - \langle q\rangle_{\rm b} \tag{24}$$

where $\theta_{\rm b}$ is the boundary layer temperature, $q_{\rm b}$ is the boundary layer moisture, and X^* represents the saturation value of the variable X. We also require that $\Lambda = \Lambda_0$ and the constants a_1 and a_2 defining P_0 in (9) satisfy $a_1 R^{-1} = a_2$. With the assumptions in (21)–(24) and ignoring the nonlinear moisture advection in (21), we arrive at the simplified moisture parametrization,

$$\frac{\partial \langle q\rangle_b}{\partial t} + \tilde{Q}\text{div } \mathbf{v}_1 = \frac{R}{\tau_e}\left(q^* - \langle q\rangle_b\right) - \tau_{\text{conv}}^{-1} P \tag{25}$$

coupled to the temperature and momentum equations for $\theta_1, \mathbf{v}_1$ in (20). These are the model parametrizations studied in Frierson et al. [16]; the interested reader can consult that paper for an alternative direct derivation directly from the equations for bulk cloud microphysics .

The derivation we have just presented above would be much more elegant if the original model retained separate equations for the boundary layer temperature, θ_b, and moisture q_b in the boundary layer. To a first approximation, most of the important fluctuations in θ_{eb} in the boundary layer for deep convective processes in the tropics involve the moisture since sensible heat fluxes are an order of magnitude smaller in the tropics [16]. This is why an equation for θ_{eb} alone is utilized for simplicity in the original multi-cloud parametrization and also partly justifies the ad hoc approximations in (24).

Finally, note that the time scale for the surface evaporative flux to affect the moisture in the free troposphere in (25) is determined by the coefficient, $R\tau_e^{-1}$. With the value $R = 1/32$ from (12) and $\tau_e \approx 8\,\text{h}$ utilized here, this evaporative time scale is about 10 days, in agreement with standard estimates [16].

4 Stability theory for an RCE to homogeneous perturbations

4.1 Radiative convective equilibrium and linear stability

A standard tool in understanding the basic properties of a convective parametrization is the linearized stability analysis at radiative convective equilibrium [8,12,13,15,34]. A radiative convective equilibrium (RCE), which is a state where the convective heating is balanced by the radiative cooling, is a time independent, static, and spatially homogeneous solution to the set of equations (1)–(11) described above. It sets up a steady state solution around which convective waves can oscillate and grow. In Khouider and Majda [37], we constructed such an RCE solution and performed a linear stability study for small wave-like perturbations from this RCE. In Sect. 5 of the present paper we elaborate on some of the remarkable physical features of unstable RCE's to homogeneous perturbations noted very briefly in Khouider and Majda [37]. To define such RCE we let

$$\begin{aligned}
&(1)\ \bar{E} = \bar{D} && (2)\ \tfrac{1}{H_T}\bar{D} = \bar{P} = \frac{1-\bar{\Lambda}}{1-\Lambda_*}\bar{P}_0\\
&(3)\ \bar{P} = \frac{2\sqrt{2}}{\pi}Q^0_{R,1} && (4)\ \left(-\bar{H}_s + \bar{H}_c\right) = \frac{2\sqrt{2}}{\pi}Q^0_{R,2}\\
&(5)\ \alpha_s\bar{P} = \bar{H}_s && (6)\ \alpha_c\frac{\bar{\Lambda}-\Lambda_*}{1-\Lambda_*}\frac{\bar{D}}{H_T} = \bar{H}_c
\end{aligned} \tag{26}$$

Given $0 < \Lambda^* < 1$ is fixed, an RCE solution with $\bar{\Lambda} < 1$ is completely determined by fixing the evaporative rate $\bar{E}$ alone provided the state of the upper troposphere is also specified by fixing $\bar{\Lambda}$ or equivalently $\bar{\theta}_{eb} - \bar{\theta}_{em}$. (When $\Lambda = \Lambda^*$ we have a pure deep convective RCE with $\bar{H}_c = 0$ and when $\Lambda^* < \Lambda < 1$ we have a mixed deep-convective–congestus RCE, see [37] for details). With the value $\theta^*_{eb} - \bar{\theta}_{eb} = 10\,\text{K}$, according to the Jordan tropical sounding [44], the realistic value of radiative cooling, $Q^0_{R,1}$, given by $\frac{2\sqrt{2}}{\pi}Q^0_{R,1} = 1\,\text{K/day}$ yields a boundary layer evaporative time scale $\tau_e \approx 8\,\text{h}$ and this is the standard value utilized below as well as in Khouider and Majda [37,39].

The linearized equations about an RCE solution are then obtained for the first order perturbation, $U(x,t) = (u_1, u_2, \theta_1, \theta_2, \theta_{eb}, q, H_s, H_c)$, and the explicit formulation of the linear system is presented in Appendix B of Khouider and Majda [37]. In such a linearized stability analysis as utilized in Sect. 4 and 5, we look for traveling wave solutions for the linearized system with the form $U(x,t) = U\exp(i(kx - \omega t))$. Here k is the wavenumber and $\omega = \omega(k)$ is the generalized dispersion relation where $\text{Re}(\omega)/k$ is the phase speed and $\text{Im}(\omega)$ is the growth of the linear wave. The detailed results are given below.

As noted recently by the authors [37], RCE's with $\bar{\theta}_{eb} - \bar{\theta}_{em}$ large enough involving mixture of deep convective and congestus clouds are unstable to homogeneous perturbations. Homogeneous solutions are special solutions of the parametrization in (17) without spatial gradients, i.e, $\left(q(t), H_c(t), H_s(t), \theta_{eb}(t), \theta_1(t), \theta_2(t)\right)$ with zero velocity components. Here we begin by briefly summarizing the results of linear theory for homogeneous perturbations of an RCE which correspond to waves with zero wavenumber ($k = 0$) in the eigenmode expansion given above. This is followed by a numerical study of the nonlinear development of the instability for instructive parameter regimes.

We consider RCE's with realistic radiative cooling $\frac{2\sqrt{2}}{\pi}Q^1_{R,0} = 1\,\mathrm{K\,day^{-1}}$ with the parameter values, $\tau_c = \tau_s = 3\,\mathrm{h}$ and $\tau_{conv} = 2\,\mathrm{h}$. The diagram showing the transition from stability to instability as the congestus parameter α_c and $\bar{\theta}_{eb} - \bar{\theta}_{em}$ vary is depicted in Fig. 1. Recall from (8) that α_c measures the strength of the congestus heating while from (5) values of $\bar{\theta}_{eb} - \bar{\theta}_{em}$ in the range $10\,\mathrm{K} < \bar{\theta}_{eb} - \bar{\theta}_{em} < 20\,\mathrm{K}$ define RCE's with mixed deep convective/congestus structure. Particularly, the relative contribution of the congestus heating at RCE increases as $\bar{\theta}_{eb} - \bar{\theta}_{em}$ increases from 10 to 20 K. This figure shows that increasing both α_c and $\bar{\theta}_{eb} - \bar{\theta}_{em}$ promotes homogeneous instability of this basic RCE. Notice that increasing both these parameters leads to the same physical situation where the congestus heating dominates at RCE. This is actually suggesting that an atmosphere dominated by lower troposphere heating from congestus clouds becomes unstable and therefore should promote deep convection. In Fig. 2, α_c is fixed at $\alpha_c = 2$ and the transition diagram is shown for varying γ_2 and $\bar{\theta}_{eb} - \bar{\theta}_{em}$. The growth contours in Figure 2 show very little variation with respect to γ_2. Recall from (9), γ_2 measures the relative contribution of second baroclinic middle troposphere temperature perturbations to deep convection. This suggests that among these parameters, α_c and $\bar{\theta}_{eb} - \bar{\theta}_{em}$ are the key parameters which control the stability of the homogeneous state RCE. Indeed, the homogeneous stability diagrams in Figs. 1 and 2 are robust and change only slightly when other parameters in the model are varied, especially, when τ_c, τ_s, τ_{conv} vary over the range in (18). Furthermore, the instability region in Figs. 1, 2 is always characterized by a single positive eigenvalue with zero phase speed which crosses through zero at the stability boundary. Under such circumstances, in the simplest scenario, one might anticipate that as the stability boundary is crossed, the nonlinear development of homogeneous perturbations to the RCE evolves to a new steady state defining an RCE with a stronger deep convective contribution, i.e, smaller $\bar{\theta}_{eb} - \bar{\theta}_{em}$. On the other hand, we have a six-dimensional set of ordinary differential equations (ODE's) so there is the possibility of much more complex dynamics involving periodic orbits and even chaotic dynamics. These possibilities are tested next.

4.2 Nonlinear homogeneous instability for the RCE

Before developing a detailed discussion, we remark that the conservation of the vertical average of equivalent potential temperature for (1) and (2) automatically yields the following conservation principle for homogeneous solutions of (17)

$$\frac{\partial}{\partial t}\left(\frac{2\sqrt{2}}{\pi}\theta_1 + q + R\theta_{eb}\right) = \frac{1}{\tau_e}\left(\theta^*_{eb} - \theta_{eb}\right) - Q^1_{R,0} - \frac{1}{\tau_R}\theta_1. \tag{27}$$

Thus, the dynamics of nonlinear perturbations are strongly constrained by (27). In particular, at any homogeneous steady state, the right hand side of (27) must vanish necessarily.

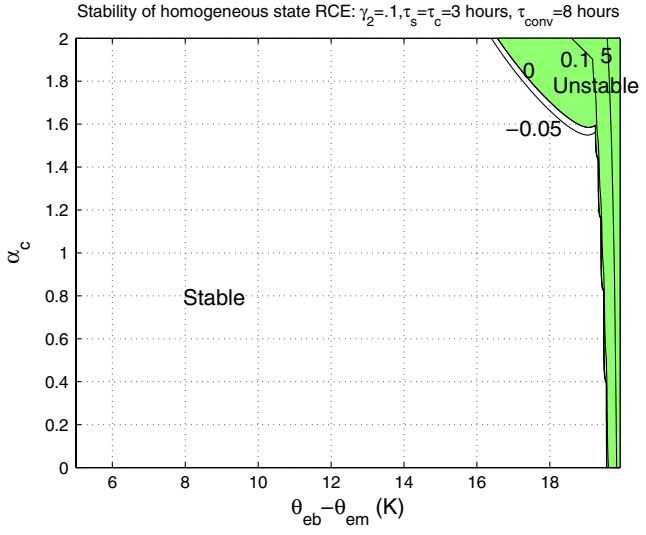

Fig. 1 Linear stability of RCE to homogeneous perturbations: bifurcation diagram in $\alpha_c - (\theta_{eb} - \theta_{em})$ plane. $\gamma_2 = 0.1$, $\tau_c = \tau_s = 3\,\mathrm{h}$, $\tau_{conv} = 2\,\mathrm{h}$. The region of instability is *shaded*

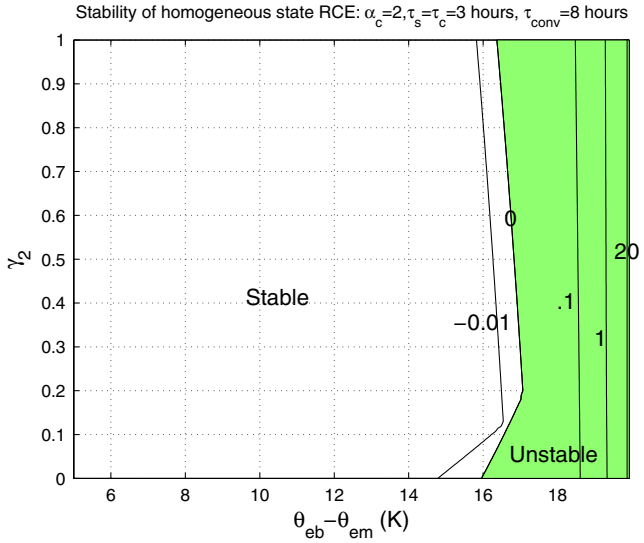

Fig. 2 Same as Fig. 1 except for axises in $\gamma_2 - \bar{\theta}_{\rm eb} - \bar{\theta}_{\rm em}$ plane and $\alpha_{\rm c} = 2$ is fixed

We did a series of elementary numerical experiments integrating the six-dimensional ODE's for $\big(q(t),\, H_{\rm c}(t),\, H_{\rm s}(t), \theta_{\rm eb}(t), \theta_1(t), \theta_2(t)\big)$ involving initial conditions which are small perturbations of homogeneous unstable RCE's for a wide range of parameter values and time scales from (18). For various parameter regimes either of the two possibilities alluded to earlier occur: either adjustment to a stable RCE or more complex dynamics with periodic and/or chaotic behavior. Three examples illustrating these regimes are presented next.

In the first example, we use the parameter values $\tau_{\rm s} = 3\,{\rm h}$, $\tau_{\rm c} = 3\,{\rm h}$, $\tau_{\rm conv} = 8\,{\rm h}$, $\gamma_2 = 0.1$ and congestus heating coefficient $\alpha_{\rm c} = 2$. The initial data is a small perturbation of the unstable RCE with $\bar{\theta}_{\rm eb} - \bar{\theta}_{\rm em} = 19.5\,{\rm K}$ yielding a relatively large second baroclinic cooling $Q^2_{R,0} = 1.65\,{\rm K/day}$ and a large congestus heating $\bar{H}_{\rm c} = 1.87\,{\rm K/day}$, at RCE. The dynamical transient behavior is depicted in Fig. 3 and illustrates the adjustment to a new stable RCE at large times with $\theta_{\rm eb} - \theta_{\rm em} = 11.87\,{\rm K}$. The adjustment process is very rapid on the order of 20–30 days for all variables except for θ_2 which adjusts more slowly over the order of 100 days on the Newtonian cooling time scale. Notice the large negative perturbed value of θ_2 in the final adjusted equilibrium which compensates for the large value of the homogeneous radiative cooling $Q^0_{R,2}$ so that $\frac{2\sqrt{2}}{\pi}(H_{\rm c} - H_{\rm s}) - Q^2_{R,0} - \frac{1}{\tau_R}\theta_2 = 0$ at equilibrium, given the large relaxation time $\tau_R = 50\,{\rm days}$ and the weaker adjusted values of $H_{\rm c}$, $H_{\rm s}$ depicted in Fig. 3.

Figure 4 illustrates the emergence of a periodic motion, with a period of roughly 100 days for θ_1, θ_2, and q and about 400 days for $\theta_{\rm eb} - \theta_{\rm em}$, from a small perturbation of an unstable RCE with $\bar{\theta}_{\rm eb} - \bar{\theta}_{\rm em} = 19.75\,{\rm K}$. The parameters here are $\tau_{\rm s} = 3\,{\rm h}$, $\tau_{\rm c} = 3\,{\rm h}$, $\tau_{\rm conv} = 2\,{\rm h}$, $\gamma_2 = 0.1$, and $\alpha_{\rm c} = 0.5$. Note that there are large fluctuations in moisture and congestus heating accompanied by a large drop in first baroclinic potential temperature, θ_1, due to radiative cooling over an interval of roughly 10 days followed by a nearly stationary but slowly decaying state of deep convection over roughly 90 days; with the radiative cooling of 1/K/day, the drop of θ_1 by roughly 10 K in 10 days is completely natural.

Finally, in Fig. 5, we present an example of transient behavior emerging from a small initial perturbation of an unstable RCE, $\bar{\theta}_{\rm eb} - \bar{\theta}_{\rm em} = 19.75$,K, with nearly periodic behavior which we conjecture is an example of heteroclinic chaotic dynamics [49,50]. Here $\tau_{\rm s} = 3\,{\rm h}$, $\tau_{\rm c} = 3\,{\rm h}$, $\tau_{\rm conv} = 8\,{\rm h}$, $\gamma_2 = 0.1$, and $\alpha_{\rm c} = 0.5$. Notice that in this case the variables θ_1, θ_2, q undergo nearly periodic motion with a mechanism very similar to that discussed earlier for the example in Fig. 4 with a much shorter lifetime for enhanced θ_1 compared with the earlier case. However, a close inspection of Fig. 5 shows that the large amplitude spikes in q and θ_1 fluctuate slightly in amplitude while there are intermittent irregular bursts and spikes in $\theta_{\rm eb} - \theta_{\rm em}$ and P[1].

[1] For the last two cases corresponding to Figs. 4 and 5, the spikes in P and $H_{\rm s}$ actually exceed the 5 K/day axis-limit and reach values respectively as large as 100 and 20 K/day and more. Such large heating rates follow naturally from the large growth rates associated with these extreme parameter regimes (see Fig. 7). The large heating values are avoided on the scales of those figures for clarity.

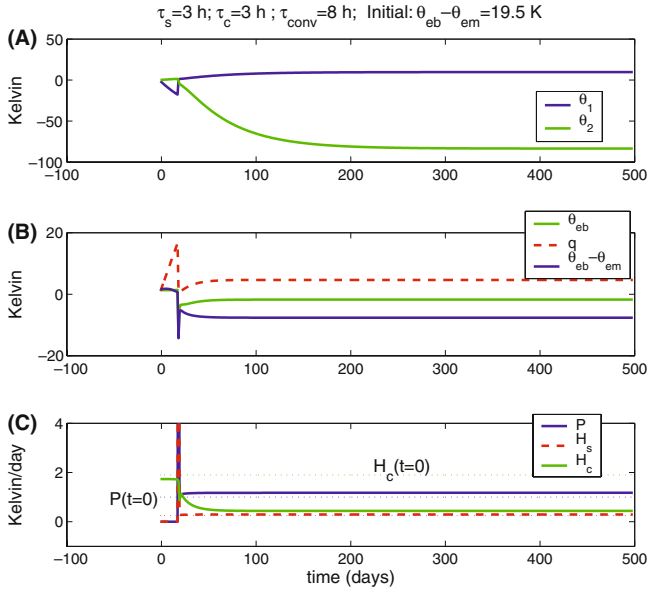

Fig. 3 Nonlinear stability of RCE to homogeneous perturbations: History of potential temperature components **a**, moist thermodynamic variables **b**, and convective heating rates **c**. The initial homogeneous RCE solution at time $t = 0$ is depicted by the *dotted lines*. Adjustment to a stable RCE: $\tau_s = \tau_c = 3\,\mathrm{h}$, $\tau_{\mathrm{conv}} = 8\,\mathrm{h}$, $\gamma_2 = 0.1$, $\alpha_c = 2$, $\bar{\theta}_{\mathrm{eb}} - \bar{\theta}_{\mathrm{em}} = 19.5\,\mathrm{K}$

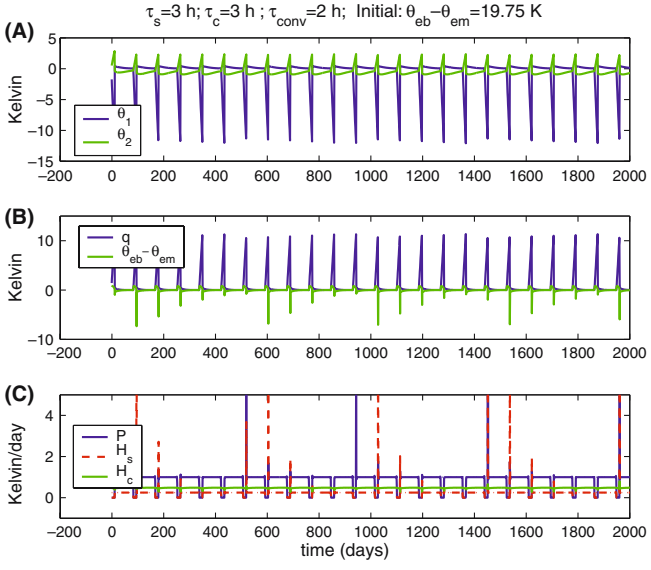

Fig. 4 Same as Fig. 3 except for the parameter values: $\tau_s = \tau_c = 3\,\mathrm{h}$, $\tau_{\mathrm{conv}} = 2\,\mathrm{h}$, $\gamma_2 = 0.1$, $\alpha_c = 0.5$, $\bar{\theta}_{\mathrm{eb}} - \bar{\theta}_{\mathrm{em}} = 19.75\,\mathrm{K}$ leading to the emergence of a periodic solution

We conclude this section by stating that the three types of behavior shown here are robust for unstable RCE's in all parameter regimes tested for the multi-cloud models.

5 Unstable moisture waves at RCE

The physical structure of linearly unstable convectively coupled waves about RCE is a basic topic of considerable interest for model convective parametrizations with crude vertical structure [8,10,12,13,15,22,34–37]. This interest arises both in providing physical structures, wavelengths, and phase speeds for comparison with observations as well as highlighting the characteristics of the convective parametrization including guidelines

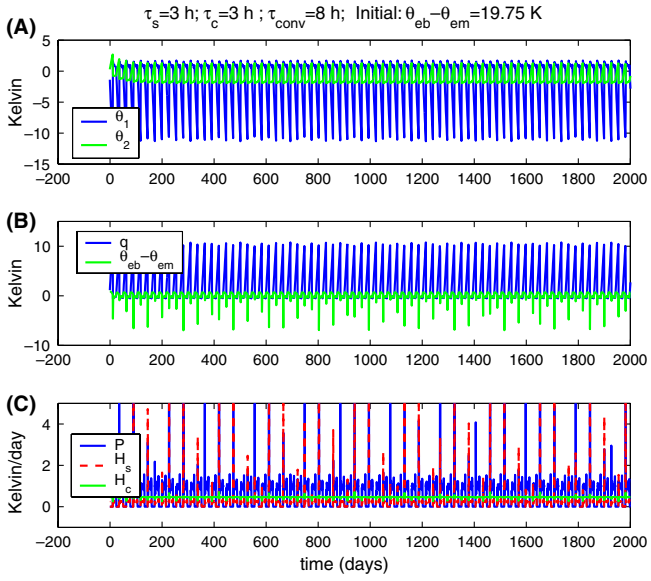

Fig. 5 Same as Figure 3 except for the parameter values: $\tau_s = \tau_c = 3\,\text{h}$, $\tau_{\text{conv}} = 8\,\text{h}$, $\gamma_2 = 0.1$, $\alpha_c = 0.5$, $\bar{\theta}_{\text{eb}} - \bar{\theta}_{\text{em}} = 19.75\,\text{K}$ leading to heteroclinic chaotic dynamics

for nonlinear simulations [35,38,39]. The nature and physical structure of the typical large scale instabilities that occur when the basic RCE is stable to homogeneous perturbations for the multicloud parametrization has already been studied by the authors elsewhere [37–39]. Here we address several issues. First, we look at sensitivity of these results when the time scales τ_c, τ_s, τ_{conv} in the parametrization vary over the range in (18); then, we document the remarkable new families of unstable waves at various wavelengths which emerge when the RCE is unstable to homogeneous perturbations.

5.1 The effect of time scales in the parametrization on instability

Here we consider the growth rate and phase speed of unstable waves for the standard RCE [37] with $\bar{\theta}_{\text{eb}} - \bar{\theta}_{\text{em}} = 14\,\text{K}$ with $\gamma_2 = 0.1$ and $\alpha_c = 0.5$. According to (18), we consider the following cases

$$\begin{aligned} &(1)\ \tau_s = \tau_c = 3\,\text{h},\ \ \tau_{\text{conv}} = 2\,\text{h} \\ &(2)\ \tau_s = \tau_c = 3\,\text{h},\ \ \tau_{\text{conv}} = 8\,\text{h} \\ &(3)\ \tau_s = \tau_c = 8\,\text{h},\ \ \tau_{\text{conv}} = 8\,\text{h} \end{aligned} \tag{28}$$

Figure 6 presents the growth rate and phase speed of the unstable waves for these three cases with the standard values in Tables 1, and 2. Here and below, the wavenumbers are calculated relative to the natural length scale $L = 40{,}000\,\text{km}$, which is the circumference of the equator while the unstable waves are marked by circles in the phase velocity diagrams. Several trends are evident; in all three cases, the instabilities are confined to scales larger than 1,500 km and are associated with phase speeds in the range of 15–25 m/s. Furthermore, successively increasing the time-scales from (1) to (2) to (3), results in smaller growth rates for this instability as might be anticipated from (17) since the amplitudes of crucial source terms are reduced. The case with $\tau_c = 1\,\text{h}$, $\tau_s = 3\,\text{h}$, $\tau_{\text{conv}} = 2\,\text{h}$ has already been discussed extensively in [37] by the authors including its detailed physical structure which strongly resembles the moist convectively coupled gravity waves seen in observations [37–39]; the physical structure of the waves in the three cases in (28) is similar and will not be repeated here.

5.2 Moisture waves for homogeneous unstable RCE's

For higher values of $\bar{\theta}_{\text{eb}} - \bar{\theta}_{\text{em}}$ for which the RCE is unstable to homogeneous perturbations, the stability and phase diagrams corresponding to Fig. 6 bifurcate drastically as $\bar{\theta}_{\text{eb}} - \bar{\theta}_{\text{em}}$ varies and display remarkably complex behavior with the emergence of other families of unstable moisture waves at various scales. Below,

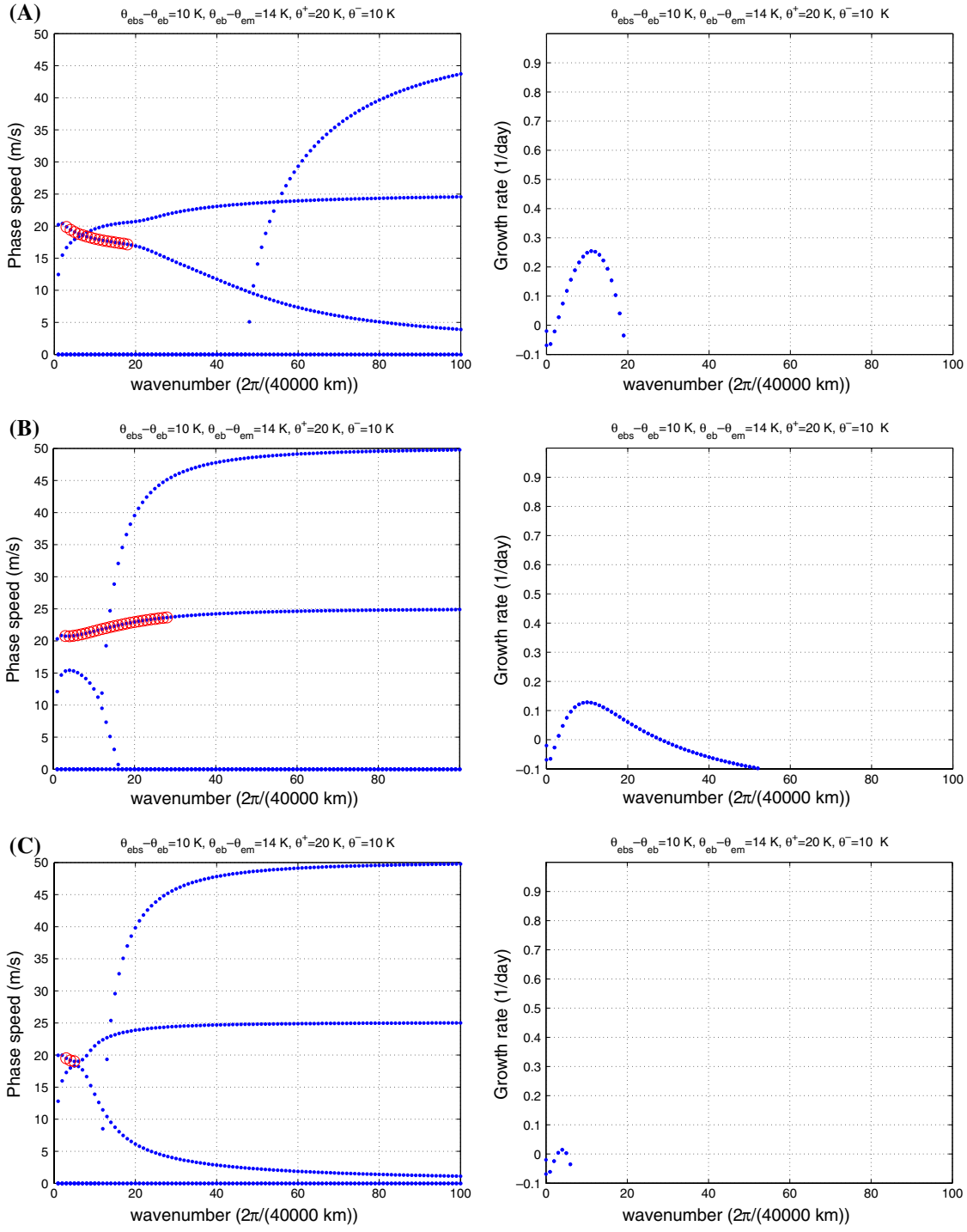

Fig. 6 Linear stability of RCE perturbations in the wavenumber domain. Growth and phase diagrams with $\bar{\theta}_{\mathrm{eb}} - \bar{\theta}_{\mathrm{em}} = 14\,\mathrm{K}$: **a** $\tau_{\mathrm{s}} = \tau_{\mathrm{c}} = 3\,\mathrm{h}$, $\tau_{\mathrm{conv}} = 2\,\mathrm{h}$; **b** $\tau_{\mathrm{s}} = \tau_{\mathrm{c}} = 3\,\mathrm{h}$, $\tau_{\mathrm{conv}} = 8\,\mathrm{h}$; **c** $\tau_{\mathrm{s}} = \tau_{\mathrm{c}} = \tau_{\mathrm{conv}} = 8\,\mathrm{h}$. Other parameters are as in Tables 1 and 2. The zero line is drawn on the top of growth diagrams to clearly separate growing from damped modes

to demonstrate this, we utilize the fixed parameters, $\tau_{\mathrm{c}} = 1\,\mathrm{h}$, $\tau_{\mathrm{s}} = 3\,\mathrm{h}$, $\tau_{\mathrm{conv}} = 2\,\mathrm{h}$, $\gamma_2 = 0.1$, $\alpha_{\mathrm{c}} = 2$ in the multicloud model and vary $\bar{\theta}_{\mathrm{eb}} - \bar{\theta}_{\mathrm{em}}$. This example is illustrative of the general behavior which occurs in particular for the three cases in (28).

Figure 7 gives the phase/instability diagrams for the increasing values $\bar{\theta}_{\mathrm{eb}} - \bar{\theta}_{\mathrm{em}} = 14, 16, 18, 18.5, 19, 19.5\,\mathrm{K}$ for the RCE; for $\bar{\theta}_{\mathrm{eb}} - \bar{\theta}_{\mathrm{em}} \geq 18.5\,\mathrm{K}$, the RCE is unstable to homogeneous perturbations. Notice that the

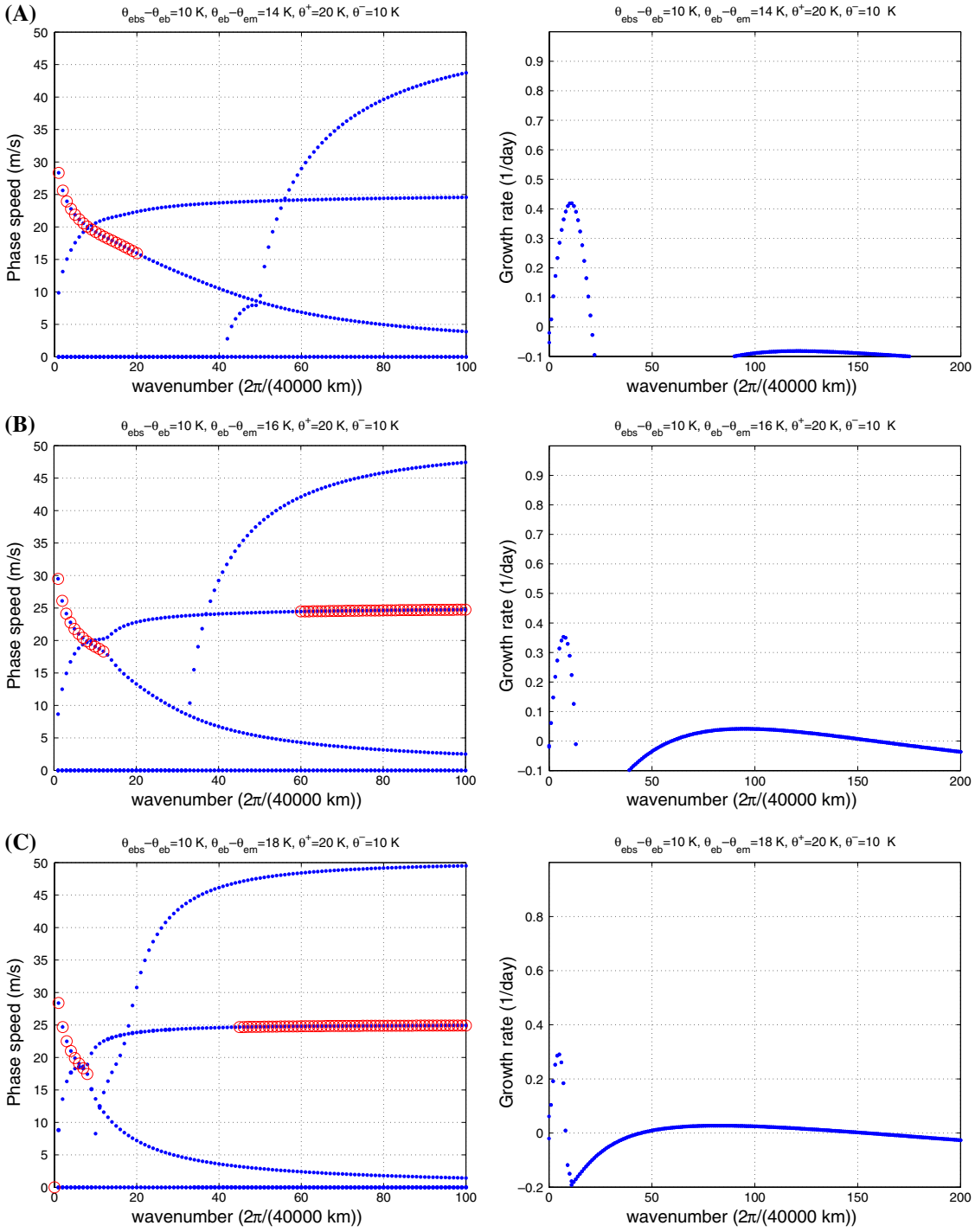

Fig. 7 Same as Fig. 6 except for $\tau_s = 3\,\text{h}$, $\tau_c = 1\,\text{h}$, $\tau_{conv} = 2\,\text{h}$, and $\alpha_c = 2$ are fixed while $\bar{\theta}_{eb} - \bar{\theta}_{em}$ varies

unstable phase diagram begins to bifurcate at $\bar{\theta}_{eb} - \bar{\theta}_{em} = 16\,\text{K}$ from the standard case at $\bar{\theta}_{eb} - \bar{\theta}_{em} = 14\,\text{K}$; at this value, a new band of unstable moist gravity waves appears at mesoscopic scales centered around 666 km (wavenumber 60) moving at essentially the dry second baroclinic gravity wave speed of 25 m/s.

The physical structure of the eastward unstable wave at wavelength 666 km is presented in Fig. 8 through bar diagrams for the unstable eigenvector component amplitudes [34,35,37] as well as traces of quantities of interest through one ad one-half spatial periods. Although this wave is moving at the second baroclinic dry

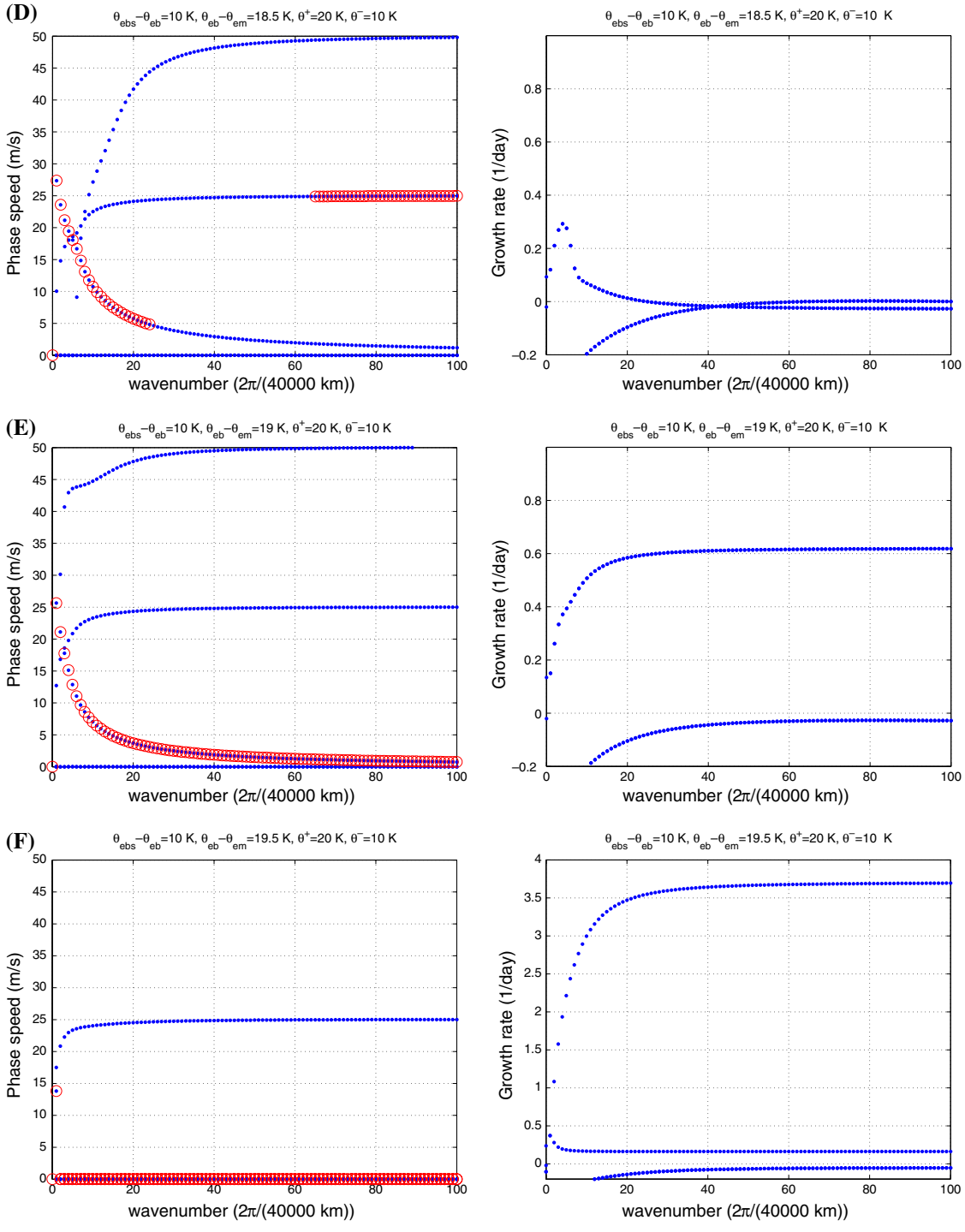

Fig. 7 Contd.

gravity wave speed and has a significant second baroclinic structure it is strongly convectively coupled with prominent moisture, congestus, stratiform, and first baroclinic mode components. It has a structure resembling those discussed by Mapes [9] which act as triggers for additional organized mesoscale convection. Furthermore, congestus peaks lead moisture peaks which lead deep convective peaks as illustrated in Figs. 8 d, e. At the value, $\bar{\theta}_{\mathrm{eb}} - \bar{\theta}_{\mathrm{em}} = 18.5\,\mathrm{K}$, a new band of slower large scale moist gravity waves emerges. Notice the

movement of the band on instability of the 25 m/s waves. For the even larger value with $\bar{\theta}_{eb} - \bar{\theta}_{em} = 19$ K there is moist gravity waves with maximum phase speed of 15 m/s on planetary to synoptic scales ($2 \leq k \leq 20$) asymptotically converging to moist gravity waves with nearly zero phase velocity and constant growth rate at small scales ($k \geq 30$) while the 25 m/s instability weakens a great deal moves back toward the small scales and ultimatly desapears.

The structure of the slow moving westward propagating moist gravity wave with wavelength 666 km and phase velocity 1.26 m/s is shown in Fig. 9; the wave is dominated by moisture and θ_{eb} fluctuations (large CAPE) and has a deep convective structure with both first and second baroclinic components with moisture

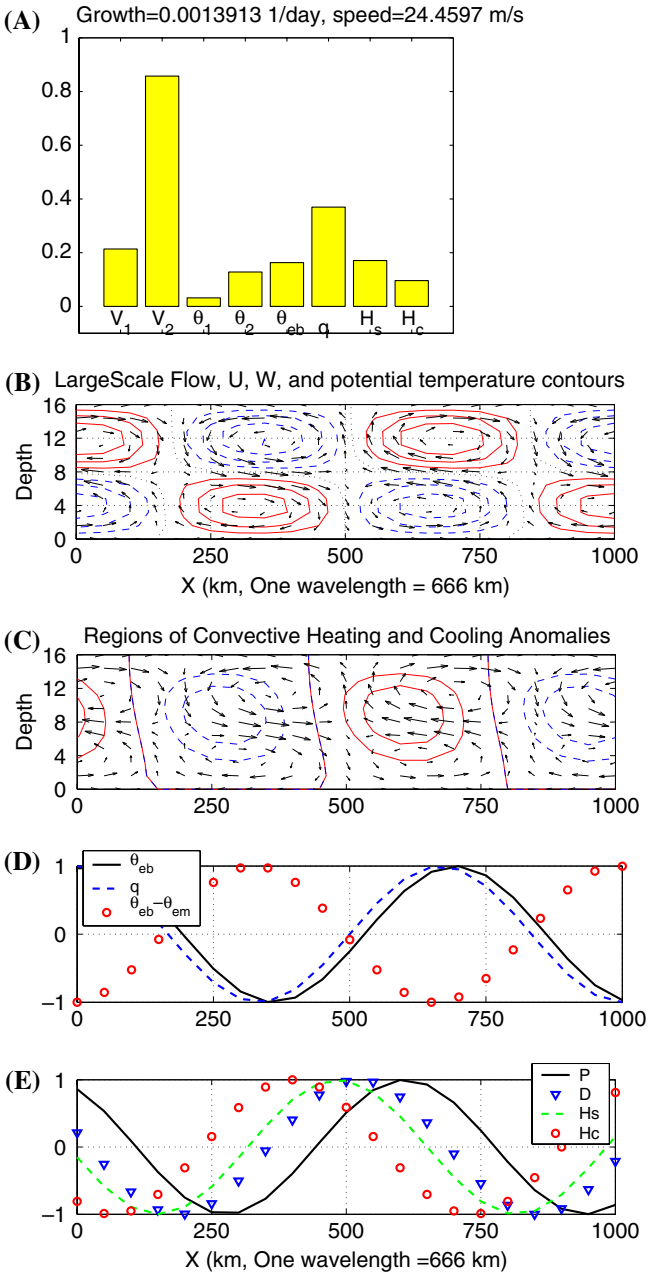

Fig. 8 Physical structure of eastward 25 m/s^{-1} moist gravity wave at wavenumber $k = 60$. $\bar{\theta}_{eb} - \bar{\theta}_{em} = 16$ K, $\tau_s = 3$ h, $\tau_c = 1$ h, $\tau_{conv} = 2$ h, $\alpha_c = 2$. Other parameters are as in Tables 1 and 2. **a** bar diagram of eigenmode component amplitudes. x-z Contours of potential temperature **b** and convective heating field **c** with velocity arrows overlaid

peaks leading deep convective peaks. (Notice from the bar diagram that u_1 is slightly larger than u_2 leading to a strong shear and strong winds near the surface and aloft.) Also because of its slow propagation speed, the slope in the (total) upward motion of nearly one (resulting from the 3 h stratiform lag: 1.26 m/s $\times$ 3 h = 13 km) is much smaller than the slope observed for the 15 m/s convectively coupled Kelvin wave analogues [34,35,37]. Given the aspect ratio on Fig. 9, this yields a nearly vertical upward motion at the center of the deep convection and an upraising of the air near the surface. These features of the slow moving wave in Fig. 9, just summarized above, including the spatial structure (strong shear, slope one of upward motion, upraising of near surface air, strong surface winds immediately in front and in the back of the convective region, etc.), the phase speed, and the length scale are reminiscent of a westward propagating squall line [46].

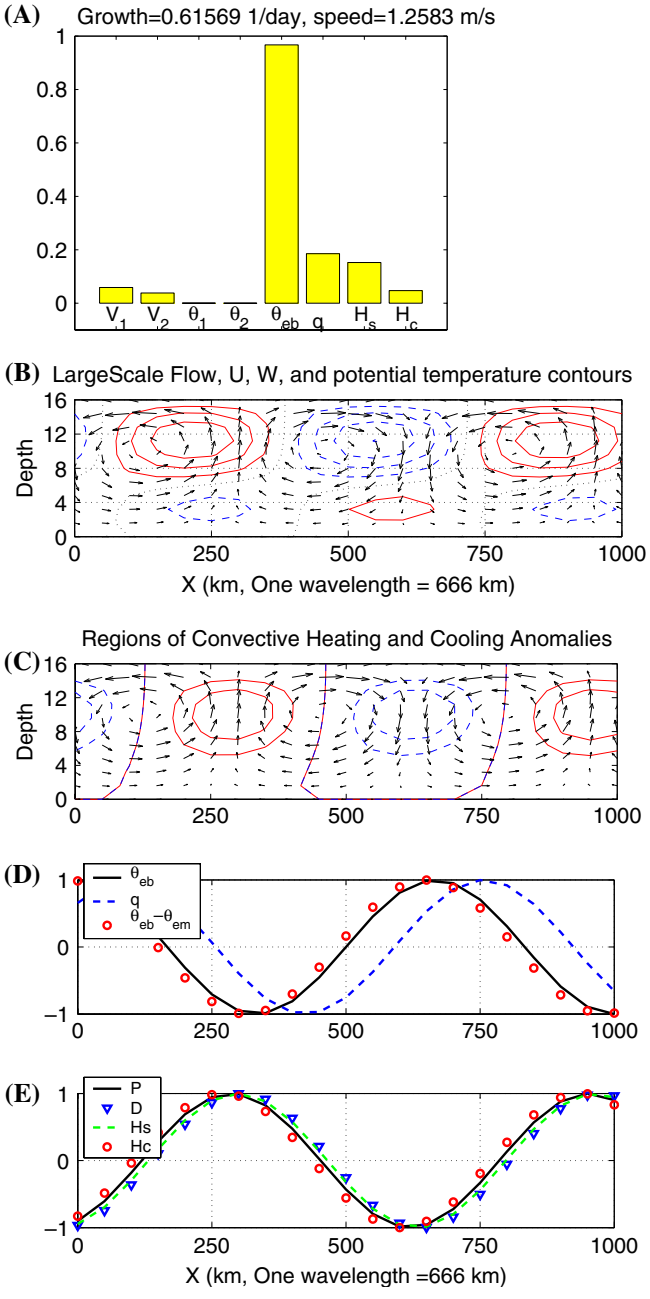

Fig. 9 Same as Fig. 8 except for the slow westward propagating moist gravity at wavenumber $k = 60$, $\bar{\theta}_{eb} - \bar{\theta}_{em} = 19$ K, $\tau_s = 3$ h, $\tau_c = 1$ h, $\tau_{conv} = 2$ h, $\alpha_c = 2$

Finally, at the largest value of $\bar{\theta}_{\rm eb} - \bar{\theta}_{\rm em} = 19.5$ K, the unstable phase diagram undergoes another bifurcation to two standing waves of instability over the entire range of wavenumber $k \geq 2$ while at wavenumber one we have the instability of two convectively coupled waves moving at roughly 13 m/s. The structure of the standing mode with the larger growth rates is shown in Fig. 10. The second standing mode has a similar structure. From Fig. 10 we see that these standing modes are essentially deep convective standing waves with the first baroclinic components dominating. Notice the air rising near the surface directly to the top of the troposphere at the locations of maximum heating and warm temperatures in Figs. 10b, c. The streamlines are on the form of Rayleigh-Benard convective cells. From Figures 10d, e, all the thermodynamic variables and forcing terms (q, $\theta_{\rm eb}$, $\theta_{\rm em}$, P, H, $H_{\rm c}$, and D) are perfectly correlated with each other confirming the non-propagating nature of the wave.

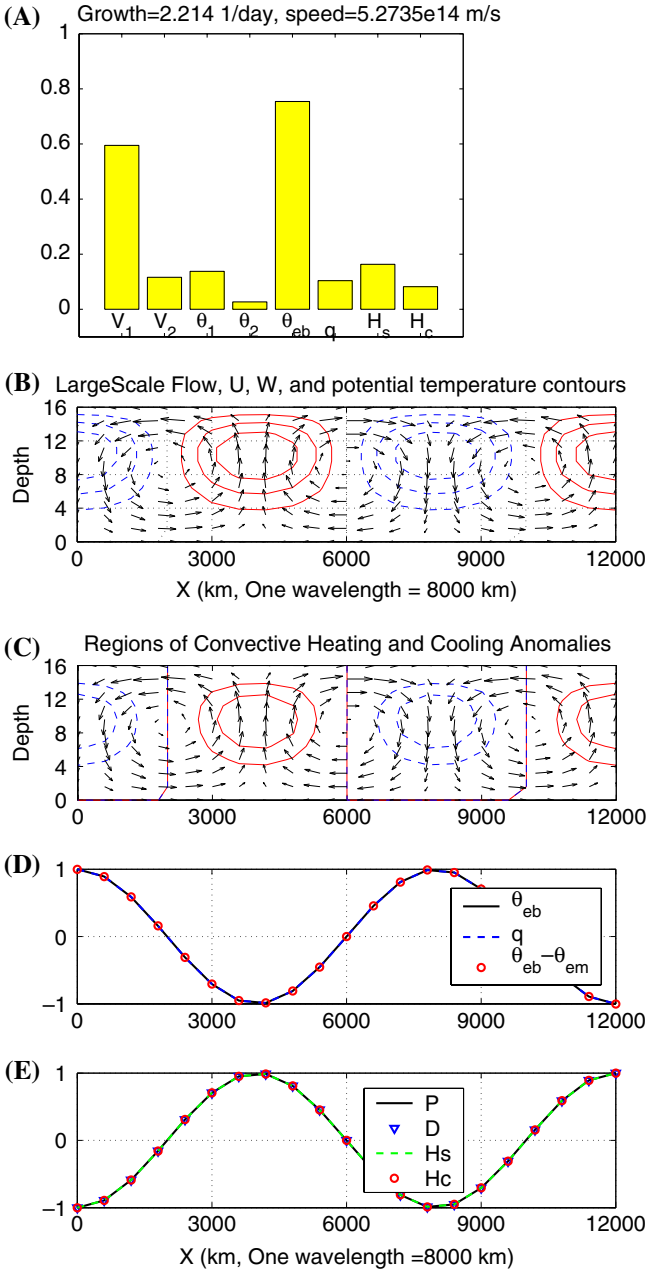

Fig. 10 Same as Fig. 9 except for $\bar{\theta}_{\rm eb} - \bar{\theta}_{\rm em} = 19.5$ K, for the standing mode with larger growth rate at wavenumber $k = 5$

6 Concluding discussion

Here we have discussed a variety of new aspects of the multicloud parametrizations with two vertical baroclinic modes introduced recently by the authors [37–39]. In Sect. 3, we clarified all of the relevant time scales in these models and showed how variants of other more familiar parametrization schemes involving a single vertical baroclinic mode arise as limiting special cases. One of the new phenomena in the multi-cloud parametrizations is the existence of suitable unstable RCE's involving a large fraction of congestus clouds and smaller fraction of deep convective clouds. Various novel aspects of the linear and nonlinear instability of such RCE's are studied here in Sects. 4, and 5. In Sect. 4, the nonlinear instability of unstable RCE's to homogeneous perturbations is studied with three different types of dynamics involving nonlinear adjustment to a deep convective dominated–stable RCE (Fig. 3), periodic oscillations (Fig. 4), and even heteroclinic chaos (Fig. 5). In Sect. 5, the linear instability of unstable RCE's to perturbations with general spatial structure is analyzed. Besides the large scale convectively coupled gravity waves [37], new modes of instability arise including mesoscale second baroclinic moist gravity waves [9], slow moving mesoscale "squall line modes", and large scale standing modes. The role of the basic convective adjustment time scales, τ_c, τ_s, τ_{conv}, on linearized stability is also clarified.

Acknowledgements The research of B.K. is supported by a University of Victoria Start-up grant and a grant from the Natural Sciences and Engineering Research Council of Canada. The research of A.M. is partially supported by ONR N0014-96-1-0043, NSF DMS-0456713, and NSF-FRG DMS-0139918. The authors are thankful to M.W. Moncrieff for sponsoring a visit for B.K. to NCAR during the summer of year 2004 where this work was partly initiated.

Appendix: Derivation of the vertically integrated moisture equation

Recall the bulk water budget equations in the atmosphere [16]

$$\begin{aligned} \frac{\partial q_v}{\partial t} + \mathrm{div}(\mathbf{V}q_v) + \frac{\partial (wq_v)}{\partial z} &= E_v - C \\ \frac{\partial q_c}{\partial t} + \mathrm{div}(\mathbf{V}q_c) + \frac{\partial (wq_c)}{\partial z} &= C - E_v - A_r \\ \frac{\partial q_r}{\partial t} + \mathrm{div}(\mathbf{V}q_r) + \frac{\partial (wq_r)}{\partial z} - \frac{\partial (v_t q_r)}{\partial z} &= A_r \end{aligned} \tag{29}$$

where q_v, q_c, q_r are the mixing ratios of water vapor, cloud water, and rain, respectively, E_v, C, A_r are the rates of evaporation, condensation, conversion of cloud water into rain, respectively, and v_t is the fall speed of precipitation (notice the minus sign in front). The quantities $\mathbf{V}$ and w represent, respectively, the horizontal and vertical (incompressible) velocity components while div denotes the horizontal divergence operator: $\mathrm{div}(u_1, u_2) = \partial_x u_1 + \partial_y u_2$.

At the large time (and spatial) scales of interest of a few days (and a few hundreds of kilometers) the dynamics of both cloud water and rain are simplified (averaged out) by assuming that clouds and rain occur at smaller scales. Therefore we assume a quasi-equilibrium where

$$\overline{A_r} = -\overline{\frac{\partial (v_t q_r)}{\partial z}} \quad \text{and} \quad \overline{C} = \overline{E}_v + \overline{A}_r$$

where the overbar represents the long-time average.

Introducing these new settings into the first equation in (30) we obtain the large scale equation for q_v:

$$\frac{\partial q_v}{\partial t} + \mathrm{div}(\mathbf{V}q_v) + \frac{\partial (wq_v)}{\partial z} = \overline{\frac{\partial (v_t q_r)}{\partial z}} \tag{30}$$

where the turbulent fluxes are ignored. Assume that the (total) water vapor, q_v, decomposes onto

$$q_v(x, y, z, t) = Q(z) + q(x, y, z, t);$$

a horizontal/time homogeneous vertical profile background (moisture stratification), $Q(z)$, plus a perturbation, q.

We introduce the vertical average of the water vapor perturbation

$$\langle q \rangle := \frac{1}{H_{\mathrm{T}}} \int_0^{H_{\mathrm{T}}} q \, \mathrm{d}z \tag{31}$$

where H_{T} is the height of the troposphere. Let P be the rate of precipitation which reaches the ground as the vertical average of the long time averaged precipitation flux :

$$P = -\frac{1}{H_{\mathrm{T}}} \int_0^{H_{\mathrm{T}}} \overline{\frac{\partial (v_{\mathrm{t}} q_{\mathrm{r}})}{\partial z}} \mathrm{d}z = \frac{1}{H_{\mathrm{T}}} \overline{v_{\mathrm{t}} q_{\mathrm{r}}} \Big|_{z=0},$$

assuming that on average q_{r} and v_{t} are zero at the top of the troposphere $z = H_{\mathrm{T}}$.

By applying the average in (31) to the equation in (30) we obtain

$$\frac{\partial \langle q \rangle}{\partial t} + \langle \mathrm{div}(\mathbf{V} q) \rangle + \left\langle w \frac{\mathrm{d}Q(z)}{\mathrm{d}z} \right\rangle + \frac{1}{H_{\mathrm{T}}} (wq) \Big|_{z=0}^{z=H_{\mathrm{T}}} = -P. \tag{32}$$

By assuming that $q(H_{\mathrm{T}}) \approx 0$; the water vapor content is negligible at the top of the troposphere, we get

$$\frac{1}{H_{\mathrm{T}}} (wq_{\mathrm{v}}) \Big|_{z=0}^{z=H_{\mathrm{T}}} \approx -\frac{1}{H_{\mathrm{T}}} (wq_{\mathrm{v}}) \Big|_{z=0} = -\frac{1}{H_{\mathrm{T}}} F_-^q$$

where F_-^q represents the net supply of water vapor from the surface. Thus the equation in (32) is rewritten as

$$\frac{\partial \langle q \rangle}{\partial t} + \langle \mathrm{div}(\mathbf{V} q) \rangle + \left\langle w \frac{\mathrm{d}Q(z)}{\mathrm{d}z} \right\rangle = F_-^q - P. \tag{33}$$

Case of two baroclinic mode models

When the governing (primitive) equations are Galerkin projected onto the first two baroclinic vertical modes plus a barotropic mode, the velocity field takes the form

$$\mathbf{V} = \bar{\mathbf{v}} + \mathbf{v}_1 \sqrt{2} \cos\left(\frac{\pi z}{H_{\mathrm{T}}}\right) + \mathbf{v}_2 \sqrt{2} \cos\left(\frac{2\pi z}{H_{\mathrm{T}}}\right)$$

and

$$w = -\frac{\sqrt{2} H_{\mathrm{T}}}{\pi} \left(\mathrm{div}\, \mathbf{v_1} \sin\left(\frac{\pi z}{H_{\mathrm{T}}}\right) + \frac{1}{2} \mathrm{div}\, \mathbf{v}_2 \sin\left(\frac{2\pi z}{H_{\mathrm{T}}}\right) \right)$$

where $\mathbf{v}_1, \mathbf{v}_2$ are, respectively, the first and second baroclinic velocity components and $\bar{\mathbf{v}}$ is the barotropic part. Plugging the formulas for $\mathbf{V}$ and w into the equation in (33) yields

$$\frac{\partial \langle q \rangle}{\partial t} + \bar{\mathbf{v}} \cdot \nabla \langle q \rangle + \mathrm{div}(\mathbf{v}_1 \phi(q)) + \mathrm{div}(\mathbf{v}_2 \psi(q)) + \tilde{Q}(\mathrm{div}\mathbf{v}_1 + \tilde{\lambda} \mathrm{div}\mathbf{v}_2) = F_-^q - P \tag{34}$$

where

$$\phi(q) = \frac{\sqrt{2}}{H_{\mathrm{T}}} \int_0^{H_{\mathrm{T}}} q \cos\left(\frac{\pi z}{H_{\mathrm{T}}}\right) \mathrm{d}z; \quad \psi(q) = \frac{\sqrt{2}}{H_{\mathrm{T}}} \int_0^{H_{\mathrm{T}}} q \cos\left(2\frac{\pi z}{H_{\mathrm{T}}}\right) \mathrm{d}z \tag{35}$$

and

$$\tilde{Q} = -\frac{\sqrt{2}}{\pi} \int_0^{H_{\mathrm{T}}} \frac{\mathrm{d}Q(z)}{\mathrm{d}z} \sin\left(\frac{\pi z}{H_{\mathrm{T}}}\right) \mathrm{d}z; \quad \tilde{\lambda} = -\frac{\sqrt{2}}{2\tilde{Q}\pi} \int_0^{H_{\mathrm{T}}} \frac{\mathrm{d}Q(z)}{\mathrm{d}z} \sin\left(\frac{2\pi z}{H_{\mathrm{T}}}\right) \mathrm{d}z. \tag{36}$$

Closures for $\phi(q)$, $\psi(q)$, $\tilde{Q}$, and $\tilde{\lambda}$ in (36)

By assuming plausible vertical profiles for $Q(z)$ and q we derive here some rough estimates for the quantities $\phi(q)$, $\psi(q)$, $\tilde{Q}$, and $\tilde{\lambda}$ in (36). We start with $\tilde{Q}$ and $\tilde{\lambda}$. The observed vertical distribution of water vapor in the tropics (for e.g. see [46] or [51]) suggests a profile for $Q(z)$ which is rapidly decreasing in the lower troposphere and asymptotically vanishing aloft. For simplicity we assume an exponential form profile,

$$Q(z) = q_0 \exp(-z/H_q), \tag{37}$$

where H_q is the e-folding distance or the moisture scale hight and q_0 a constant representing the value of q at the surface $z = 0$. We have, from (36),

$$\tilde{Q} = \frac{\sqrt{2}q_0}{\pi H_q} \int_0^{H_\mathrm{T}} \mathrm{e}^{-z/H_q} \sin\left(\frac{\pi z}{H_\mathrm{T}}\right) \mathrm{d}z = \frac{\sqrt{2}q_0}{H_\mathrm{T}/H_q + \pi^2 H_q/H_\mathrm{T}} \left(1 + \mathrm{e}^{-H_\mathrm{T}/H_q}\right)$$

and

$$\tilde{\lambda}\tilde{Q} = \frac{\sqrt{2}q_0}{2\pi H_q} \int_0^{H_\mathrm{T}} \mathrm{e}^{-z/H_q} \sin\left(\frac{2\pi z}{H_\mathrm{T}}\right) \mathrm{d}z = \frac{\sqrt{2}q_0}{H_\mathrm{T}/H_q + 4\pi^2 H_q/H_\mathrm{T}} \left(1 - \mathrm{e}^{-H_\mathrm{T}/H_q}\right), \tag{38}$$

which yield

$$\tilde{\lambda}(H_q/H_\mathrm{T}) = \frac{1 + \pi^2 (H_q/H_\mathrm{T})^2}{1 + 4\pi^2 (H_q/H_\mathrm{T})^2} \tanh\left(\frac{1}{2H_q/H_\mathrm{T}}\right);$$

a monotonically decreasing function of H_q/H_T with the upper-bound

$$\tilde{\lambda} \leq \lim_{H_q/H_\mathrm{T} \longrightarrow 0} \tilde{\lambda}(H_q/H_\mathrm{T}) = 1,$$

if for the example $H_q/H_\mathrm{T} = 1/8$, then we get $\tilde{\lambda} = 0.7135$. Therefore, values of $\tilde{\lambda}$ ranging from $\tilde{\lambda} = 0.7$ to $\tilde{\lambda} = 1$ are plausible, in our case we pick the conservative value of $\tilde{\lambda} = 0.8$. Moreover, note that $\tilde{Q}$ depends linearly on the surface moisture q_0 therefore it can take any arbitrary value. For our calculations we use the standard value of $\tilde{Q} = 0.9$ also used in [16,42,43,52].

Now we return to $\phi(q)$ and $\psi(q)$. We seek closures on the form

$$\phi(q) = \tilde{\alpha}_1 \langle q \rangle; \quad \text{and} \quad \psi(q) = \tilde{\alpha}_2 \langle q \rangle \tag{39}$$

where $\tilde{\alpha}_1$ and $\tilde{\alpha}_2$ are constants. We assume separation of variables

$$q(x, y, z, t) = q_1(z) q_2(x, y, t). \tag{40}$$

Therefore

$$\langle q \rangle = \langle q_1 \rangle \, q_2, \tag{41}$$

then provided that $\langle q_1 \rangle \neq 0$, we have

$$\tilde{\alpha}_1 = \frac{\sqrt{2}}{H_\mathrm{T} \langle q_1 \rangle} \int_0^{H_\mathrm{T}} q_1(z) \cos\left(\frac{\pi z}{H_\mathrm{T}}\right) \mathrm{d}z,$$

and

$$\tilde{\alpha}_2 = \frac{\sqrt{2}}{H_\mathrm{T} \langle q_1 \rangle} \int_0^{H_\mathrm{T}} q_1(z) \cos\left(\frac{2\pi z}{H_\mathrm{T}}\right) \mathrm{d}z.$$

If we assume that the bulk of the moisture variability is concentrated within the lower half $0 \leq z \leq H_{\mathrm{T}}/2$ of the troposphere then we can apply the mean value theorem for the first integral and get

$$\tilde{\alpha}_1 \approx \frac{\sqrt{2}}{H_{\mathrm{T}} \langle q_1 \rangle} \int_0^{H_{\mathrm{T}}/2} q_1(z) \cos\left(\frac{\pi z}{H_{\mathrm{T}}}\right) \mathrm{d}z = \frac{q_1(z_l)\sqrt{2}}{H_{\mathrm{T}} \langle q_1 \rangle} \int_0^{H_{\mathrm{T}}/2} \cos\left(\frac{\pi z}{H_{\mathrm{T}}}\right) \mathrm{d}z \approx \frac{2\sqrt{2}}{\pi} = 0.9003 \approx 1.$$

where $0 \leq z_l \leq H_{\mathrm{T}}/2$ and we assumed $\langle q_1 \rangle \approx q_1(z_l)$ to a first approximation. For $\tilde{\alpha}_2$, we use a simple midpoint quadrature rule on the lower half of the troposphere leading to

$$\tilde{\alpha}_2 \approx \frac{\sqrt{2}}{H_{\mathrm{T}} \langle q_1 \rangle} \int_0^{H_{\mathrm{T}}/2} q_1(z) \cos\left(\frac{2\pi z}{H_{\mathrm{T}}}\right) \mathrm{d}z \approx \frac{\sqrt{2}}{2} \frac{q_1(H_{\mathrm{T}}/4)}{\langle q_1 \rangle} \cos\left(\frac{\pi}{2}\right) = 0.$$

The extreme situation where the above approximation would fail occurs when $q_1(z)$ is correlated with $\cos(\frac{2\pi z}{H_{\mathrm{T}}})$, i.e, $q_1(z) \approx q_0 \cos(\frac{2\pi z}{H_{\mathrm{T}}})$. This yields

$$\langle q_1 \rangle \approx 0$$

in which case our assumption $\langle q_1 \rangle \neq 0$ is not valid thus leading to undetermined values for $\tilde{\alpha}_1, \tilde{\alpha}_2$. Nevertheless, we believe that such a situation is very unlikely in nature and therefore, overall, we will have an effective $\tilde{\alpha}_2 << 1$. Therefore, in our nonlinear simulations using the system in (1), we use the values

$$\tilde{\alpha}_1 = 1, \quad \tilde{\alpha}_2 = 0.1.$$

With the values of $\tilde{\lambda}, \alpha_1, \alpha_2$ given, (34) yields the moisture equation used in the multicloud parametrizations with the angle brackets omitted for simplicity in exposition.

References

1. Nakazawa, T.: Tropical super clusters within intraseasonal variations over the western pacific. J. Meteorol. Soc. Jpn. **66**, 823–839 (1988)
2. Hendon, H.H., Liebmann, B.: Organization of convection within the Madden–Julian oscillation. J. Geophys. Res. **99**, 8073–8083 (1994)
3. Wheeler, M., Kiladis, G.N.: Convectively coupled equatorial waves: Analysis of clouds and temperature in the wavenumber-frequency domain. J. Atmos. Sci. **57**, 613–640 (1999)
4. Emanuel, K.A., Raymond, D.J.: The representation of Cumulus convection in numerical models. In: Meteorological monographs, vol. 84, Boston: American Meterological Society, 1993
5. Smith, R.K: The physics and parametrization of moist atmospheric convection. NATO ASI, Kluwer, Dordrecht, 1997
6. Slingo, J.M. et al.: Intraseasonal oscillation in 15 atmospheric general circulation models: results from an amip diagnostic subproject. Climate Dyn. **12**, 325–357 (1996)
7. Moncrieff, M.W., Klinker, E.: Organized convective systems in the tropical western pacific as a process in general circulation models: a toga-coare case study. Q. J. Roy. Meteorol. Soc. **123**, 805–827 (1997)
8. Emanuel, K.A.: An air-sea interaction model of intraseasonal oscillations in the tropics. J. Atmos. Sci. **44**, 2324–2340 (1987)
9. Mapes, B.E.: Gregarious tropical convection. J. Atmos. Sci. **50**, 2026–2037 (1993)
10. Neelin, D., Yu, J.: Modes of tropical variability under convective adjustment and the Madden–Julian oscillation. Part I: analytical theory. J. Atmos. Sci. **51**, 1876–1894 (1994)
11. Yano, J.-I., McWilliams, J., Moncrieff, M., Emanuel, K.A.: Hierarchical tropical cloud systems in an analog shallow-water model. J. Atmos. Sci. **48**, 1723–1742 (1995)
12. Yano, J.-I., Moncrieff, M., McWilliams, J.: Linear stability and single-column analyses of several cumulus parametrization categories in a shallow-water model. Q. J. Roy. Meteorol. Soc. **124**, 983–1005 (1998)
13. Majda, A., Shefter, M.: Waves and instabilities for model tropical convective parametrizations. J. Atmos. Sci. **58**, 896–914 (2001)
14. Majda, A.J., Khouider, B.: Stochastic and mesoscopic models for tropical convection. Proc. Natl. Acad. Sci. USA **99**, 1123–1128 (2002)
15. Fuchs, Z., Raymond, D.: Large-scale modes of a nonrotating atmosphere with water vapor and cloud-radiation feedbacks. J. Atmos. Sci. **59**, 1669–1679 (2002)
16. Frierson, D., Majda, A., Pauluis, O.: Dynamics of precipitation fronts in the tropical atmosphere: a novel relaxation limit. Commun. Math. Sci. **2**, 591–626 (2004)
17. Charney, J.G., Eliassen, A.: On the growth of the hurricane depression. J. Atmos. Sci. **21**, 68–75 (1964)
18. Yamasaki, M.: Large-scale disturbances in a conditionally unstable atmosphere in low latitudes. Pap. Meteor. Geophys. **20**, 289–336 (1969)

19. Hayashi, Y.: Large-scale equatorial waves destabilized by convective heating in the presence of surface friction. J. Meteor. Soc. Jpn. **49**, 458–466 (1971)
20. Lindzen, R.S.: Wave-cisk in the tropics. J. Atmos. Sci. **31**, 156–179 (1974)
21. Arakawa, A., Shubert, W.H.: Interaction of a cumulus cloud ensemble with the large-scale environment. Part i. J. Atmos. Sci. **31**, 674–701 (1974)
22. Emanuel, K.A., Neelin, J.D., Bretherton, C.S.: On large-scale circulations in convecting atmosphere. Q. J. Roy. Meteor. Soc. **120**, 1111–1143 (1994)
23. Lin, X., Johnson, R.H.: Kinematic and thermodynamic characteristics of the flow over the western pacific warm pool during toga coare. J. Atmos. Sci. **53**, 695–715 (1996)
24. Johnson, R.H., Rickenbach, T.M., Rutledge, S.A., Ciesielski, P.E., Schubert, W.H.: Trimodal characteristics of tropical convection. J. Climate **12**, 2397–2407 (1999)
25. Straub, K.H., Kiladis, G.N., Observations of a convectively-coupled kelvin wave in the eastern pacific itcz. J. Atmos. Sci. **59**, 30–53 (2002)
26. Haertl, P.T., Kiladis, G.N.: On the dynamics of two day equatorial disturbances. J. Atmos. Sci. **61**, 2707–2721 (2004)
27. Kiladis, G.N., Straub, K.H., Haertl, P.: Zonal and vertical structure of the Madden–Julian oscillation. J. Atmos. Sci. **62**, 2790–2809 (2005)
28. Dunkerton, T.J., Crum, F.X.: Eastward propagating 2- to 15-day equatorial convection and its relation to the tropical intraseasonal oscillation. J. Geophys. Res. **100**, 25781–25790 (1995)
29. Majda, A., Biello, J.: A multi-scale model for the intraseasonal oscillation. Proc. Natl. Acad. Sci. **101**, 4736–4741 (2004)
30. Biello, J., Majda, A.: A multi-scale model for the madden–julian oscillation. J. Atmos. Sci. **62**, 1694–1721 (2005)
31. Zehnder, J.: A comparison of convergence- and surface-flux-based convective parametrizations with applications to tropical cyclogenesis. J. Atmos. Sci. **58**, 283–301 (2001)
32. Craig, G.C., Gray, S.L.: CISK or WISHE as the mechanism for tropical cyclone intensification. J. Atmos. Sci. **53**, 3528–3540 (1996)
33. Mapes, B.E.: Convective inhibition, subgridscale triggering energy, and "stratiform instability" in a toy tropical wave model. J. Atmos. Sci. **57**, 1515–1535 (2000)
34. Majda, A., Shefter, M.: Models for stratiform instability and convectively coupled waves. J. Atmos. Sci. **58**, 1567–1584 (2001)
35. Majda, A., Khouider, B., Kiladis, G.N., Straub, K.H., Shefter, M.: A model for convectively coupled tropical waves: nonlinearity, rotation, and comparison with observations. J. Atmos. Sci. **61**, 2188–2205 (2004)
36. Yano, J.-I., Emanuel, K.: An improved model of the equatorial troposphere and its coupling to the stratosphere. J. Atmos. Sci. **18**, 377–389 (1991)
37. Khouider, B., Majda, A.J.: A simple multicloud parametrization for convectively coupled tropical waves. Part i: linear analysis. J. Atmos. Sci. **63** pp. 1308–1323 (2006)
38. Khouider, B., Majda, A.J.: A simple multicloud parametrization for convectively coupled tropical waves. Part ii: nonlinear simulations. J. Atmos. Sci. (2006, in press)
39. Khouider, B., Majda, A.J.: Model multicloud parametrizations for convectively coupled waves: detailed nonlinear wave evolution. Dynam. Atmos. Oceans (2006, in press)
40. Neelin, D., Zeng, N.: A quasi-equilibrium tropical circulation model–formulation. J. Atmos. Sci. **57**, 1741–1766 (2000)
41. Majda, A., Biello, J.: The nonlinear interaction of barotropic and equatorial baroclinic Rossby waves. J. Atmos. Sci. **60**, 1809–1821 (2003)
42. Khouider, B., Majda, A.J.: A non-oscillatory well balanced scheme for an idealized tropical climate model. Part I: Algorithm and validation. Theor. Comput. Fluid Dyn. **19**, 331–354 (2005)
43. Khouider, B., Majda, A.J.: A non-oscillatory well balanced scheme for an idealized tropical climate model. Part II: Nonlinear coupling and moisture effects. Theor. Comput. Fluid Dyn. **19**, 355–375 (2005)
44. Gill, A.: Atmosphere-ocean dynamics. International geophysics series, vol. 30. Academic, New York, (1982)
45. Betts, A.K., Miller, M.J.: A new convective adjustemnt scheme. Part ii: single column tests using gate wave, bomex, and arctic air-mass data sets. Q. J. Roy. Meteorol. Soc. **112**, 693–709 (1986)
46. Emanuel, K.: Atmospheric convection. Oxford University Press, Oxford, (1994)
47. Betts, A.K.: A new convective adjustemnt scheme. part i: Observational and theoretical basis. Q. J. Roy. Meteorol. Soc. **112**, 677–692 (1986)
48. Bretherton, C.S., Peters, M.E., Back, L.E.: Relationship between water vapor path and precipitation over the tropical oceans. J. Climate **17**, 1517–1528 (2004)
49. Armbuster, D.J., Guckenheimer, J., Holmes, P.: Heteroclinic cycles and modulated traveling waves in systems with $\mathcal{O}(2)$ symmetry. Phys. D **29**, 257–282 (1988)
50. Holmes, P., Lumley, J.L., Berkooz, G.: Turbulence, coherent structures, dynamical systems, and symmetry. Cambridge University Press, New York, (1996)
51. Pruppacher, H.R, Klett, J.D.: Microphysics of clouds and precipitation, chap 12. Kluwer, Dordrecht, (2000)
52. Lin, J., Neelin, J.D., Zeng, N.: Maintenance of tropical intraseasonal variability: Impact of evaporation-wind feedback and midlatitude storms. J. Atmos. Sci. **57**, 2793–2823 (2000)